UNIVERSITY OF CALIFORNIA
RIVERSIDE

Synthesis, Characterization, and Exfoliation of Ternary Layered Borides

A Thesis submitted in partial satisfaction
of the requirements for the degree of

Master of Science

in

Chemistry

by

Ryland Forsythe

June 2018

Thesis Committee:
Dr. Boniface Fokwa, Chairperson
Dr. Gregory Beran
Dr. Matthew Conley

The Thesis of Ryland Forsythe is approved:

_____

_____

_____

Committee Chairperson

University of California, Riverside

Acknowledgements

The text of this or thesis, in part or in full, is a reprint of the material as it appears in Eur. J. Inorg. Chem. 10.1002/ejic.201800235 [HT-NbOsB: Experimental and Theoretical Investigations of a New Boride Structure Type Containing Boron Chains and Isolated Boron Atoms, Authors: Ryland Forsythe, Jan P. Scheifers, Yuemei Zhang, and Boniface Tsinde Polequin Fokwa, © 2018 WILEY-VCH Verlag GmbH & Co. KGaA, Weinheim]. The co-author (Boniface Tsinde Polequin Fokwa) listed in that publication directed and supervised the research which forms the basis for this thesis. Jan P. Scheifers provided expertise in crystallography, powder X-ray diffraction, and intermetallic boride chemistry. Yuemei Zhang provided expertise in density functional theory and interpretation of calculated data. This work was supported by the National Science Foundation Career award to BPTF (no. DMR-1654780). We thank San Diego Supercomputer Center (SDSC) for providing computational resources.

On a personal note, I would like to thank first my parents and sister. They have been nothing but supportive, even if they don't understand what it is I actually do. I would like to thank Boniface for giving me the opportunity to work in his lab and learn from him, as well as my fellow lab mates who have taught me so much these last two years. They

have been not only good coworkers, but good people and good friends to me, and have made my residence here much better.

Table of Contents

List of Figures

List of Tables

Chapter 1: Introduction

The family of metal-rich borides displays a staggering array of crystal structures which exhibit diverse chemical and physical properties, and are increasingly gathering the attention of solid-state chemists, material scientists and physicists. Some properties common to intermetallic borides include high hardness including superhardness (>40GPa),[1] high melting points (typically in excess of 2,000 ^{o}C), and high chemical inertness. There are also many borides that exhibit more unique properties such as: superconductivity (MgB_2),[2] exceptional catalytic activity (MoB_2),[3] and interesting magnetic properties such as itinerant ferromagnetism or magnetic frustration (Fe_2AlB_2 and $TiCrIr_2B_2$ respectively).[4] In many cases the density of states (DOS) exhibits a pseudogap near the Fermi level E_f, which acts as a stability window within which the Fermi level can be shifted. Alternatively, a peak in the DOS can be targeted to induce an electronic instability, possibly leading to structural or electronic distortions. This allows for elements with different numbers of valence electrons to be substituted onto different atomic positions and it becomes possible, for example, to substitute a magnetically active element into a specific position. New phases can be rationally

designed, to a degree, by using a known crystal structure to elicit specific properties. [1,5–7]

Synthesis of intermetallic borides poses a few substantial hurdles to overcome. The most common technique involves mixing powders of the individual elements, using a press to compact them, and then melting the resulting pellet. Due to the aforementioned melting temperature of most borides, this necessitates extreme conditions such as arc melting. This involves passing a high current, usually 10-50 amps, from an electrode through the sample and into a water cooled copper crucible. Although borides are quite chemically stable, upwards of 1500 ^{o}C even they need to be protected from oxidation in an inert atmosphere. A side effect of this synthesis process is the rapid cooling rate, which enables synthesis of compounds that would be inaccessible through processes closer to equilibrium. To overcome the large temperatures needed for solid state diffusion, molten metal fluxes can be used as a solvent to increase diffusion rates. This has the added benefit of facilitating large single crystal growth, which is ideal in many cases including structure determination and properties measurement. Other methods include the reduction of metal oxides by boron (sometimes including carbon), chemical vapor deposition, and solid-state metathesis.[8]

Boron tends to form covalent compounds, while it's electron deficiency lends itself to unusual multicenter bonds; this combination results in complex structures containing boron fragments and extended networks. There are many common structural motifs in these compounds, mainly controlled by the metal to boron ratio. Isolated boron atoms tend to occur in high M:B ratios, such as in the M_3B (M=Re, Tc) or $Ti_3Co_5B_2$ type structures.[9,10] These isolated boron atoms are commonly found at the center of a trigonal prism made up of metal atoms (MB_6). At lower M:B ratios, around 2:1, more diverse boron fragments are formed, such as B_2 dumbbells, B_4 and B_5 [11] chain fragments, trigonal planar B_4 fragments, or B_6 rings.[5] In all these cases, the metal atoms form an arrangement of trigonal prisms, which are connected by a shared rectangular face. This allows boron atoms to form covalent B-B bonds. If all those prisms then share two of their rectangular faces with neighboring prisms at a 1:1 metal to boron ratio, infinite zig zag boron chains are formed such as in the FeB, CrB, and MoB structure types.[12] In MoB alternating boron chains are arranged perpendicularly to each other, in contrast to the parallel arrangement in CrB and FeB. The chains in FeB are canted with respect to each other, compared to the CrB chains which are all zig zag along the same direction. For even lower M:B ratios [13,14]

boron layer and 3D boron cluster networks [15] are observed. In all cases these M:B ratios serve as guidelines more than rules.

Moving from binary systems to ternaries and beyond, the picture becomes even more complex. Due to different electronegativities, sizes, affinities, etc., between the metals different boron fragments can form with each metal, which allows for an interesting fragment-based approach to these systems. Many combinations have been previously reported, including isolated boron atoms inside trigonal prisms together with most of the fragments listed above. A few examples include $Re_5Co_2B_4$ (isolated B and B_2 dumbbells) [16], $Ti_7Rh_4Ir_2B_8$ (isolated B and B_6 rings)[17], and $Ti_{1+x}Rh_{2-x+y}Ir_{3-y}B_3$ (isolated B and zig-zag B_4 units).[18] Recently, the NbOsB ternary compound was reported to crystallize with the $Ti_{1+x}Rh_{2-x+y}Ir_{3-y}B_3$ structure type.[19]

In the regime from a 4:1 M:B to a 1:2 M:B ratio, the most common boron fragments are not 3D in nature, but rather exhibit a reduced dimensionality. The planar B_4 and B_6 ring fragments are both 2D, while the chain fragments from B_2 dumbbells up to infinite boron chains are quasi 1D. These fragments typically are seen sharing the same plane of the crystal structure, as a result of the trigonal prism layering. In some cases however, the trigonal prisms are not in direct contact on

their triangular face, and there is an alternating layer between these prisms containing the boron fragments. Examples include Cr_2AlB_2 and MoAlB, which feature a single and double layer, respectively, of aluminum separating each layer of trigonal prisms and infinite boron chains.[20,21]

Recently the M_nAB_n (M=transition metal, A=group 13 element, B=boron) class of compounds [20,22] have attracted attention due to their similarity to MXene starting phases. MXenes are a class of 2D materials first developed by Michael Naguib with Drs. Yury Gogotsi and Michel Barsoum at Drexel University in 2011.[23] They are created by etching out the A layer of layered $M_{n+1}AX_n$ phases (M=transition metal, A=group 14 or 15 element, X=C,N) with n=1, 2, or 3, resulting in loose stacks of MX slabs. These $M_{n+1}AX_n$ phases belong to the $P6_3/mmc$ space group and are composed of two formula units per unit cell, where M layers are distorted edge sharing octahedra, with X atoms filling all the octahedral sites, and strong covalent bonding within the MX layers. These MX layers share metallic bonds with alternating A layers, forming a laminate structure. There are currently over 70 ternary compounds that share this structure for just A=Al, leaving the possibility for synthesizing a wide variety of 2D materials by delamination.[24]

The first synthesis was achieved by using an aqueous solution of HF acid at room temperature to selectively etch the A layer while leaving the $M_{n+1}X_n$ layer unaffected. Subsequent work has refined this procedure, such as in-situ formation of HF using HCl and fluoride salts to reduce the concentration and harshness of the solution, or on using eutectic molten fluoride salt mixtures.[2] Due to relatively large interlayer interactions compared to graphite or layered sulfides, it is necessary to first intercalate the structure to achieve delamination. The intercalant of choice is typically a polar or basic organic molecule, or a metal cation. Often, little additional agitation is needed to exfoliate the layers, leading to single or few layer flakes in a colloidal solution. [25]

The MXenes have a range of interesting properties depending on composition, surface termination, and synthesis conditions.[26–28] Many are initially metallic, but develop a tunable bandgap based on the surface termination. Some MXenes have been predicted to be topological insulators and others to have magnetic properties, although the latter excludes surface terminations.[28] Many have demonstrated outstanding results as battery electrodes or capacitors,[29] due to a combination of high conductivity and band dispersion as well as a large surface area. Other potential applications

include polymer composites, water purification, catalysis, and photothermal conversion.[30–32]

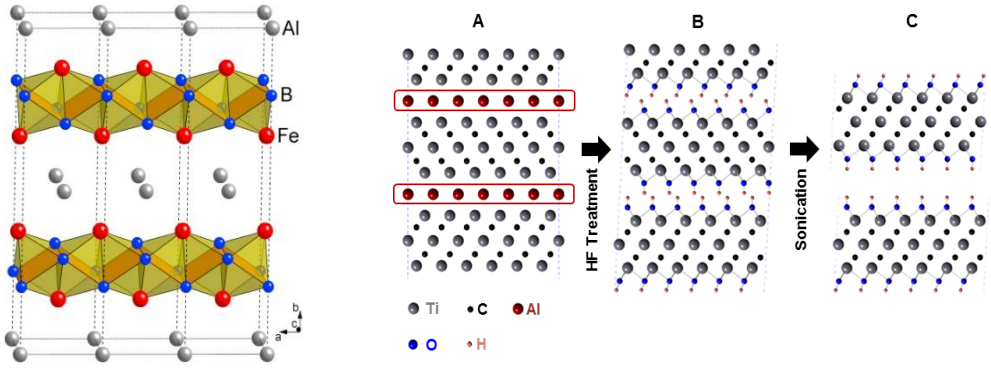

Figure 1.1 Left: The AlM_2B_2 (M=Cr, Mn, Fe) structure. Right: The process for turning a MAX phase into MXene sheets, and representative structures at each step.[1]

More recently a similar class of compounds have attracted attention: M_nAB_n (B=boron) phases[20,22] have a similar layering structure, and also show anisotropic properties. These phases are orthorhombic instead of hexagonal and so far, always exhibit C centering. In contrast with the MAX phases, the borides feature boron sitting in metal trigonal prisms which are sharing two rectangular faces with adjacent prisms, while the third face is centered on the aluminum atom in the next layer. The boron network forms a corrugated 2D sheet within the MB layer with each boron atom coordinated to an aluminum atom through the rectangular face of the metal trigonal

prism. This leads to an increased interaction between the boron and aluminum atoms, compared with the MAX phases which has carbon interacting with aluminum through the triangular face of the octahedra it sits in. In the case M_nAB_n (n=1) e.g. MoAlB, the aluminum forms a double layer between each MB layer. In cases where n is one greater than the amount of aluminum, e.g. Cr_2AlB_2, Cr_3Al2B_3, and Cr_4Al3B_4, aluminum forms a single layer between each MB layer.

The bulk boride phases possess a couple properties unique from the MAX phases, including high temperature stability and outstanding hardness.[33] Of particular interest is Fe_2AlB_2, which is both an itinerant ferromagnet and magnetocaloric.[34] They also pose unique challenges for exfoliation, including reduced chemical inertness to acid and stronger Al-MB interactions.[35] There is currently a dearth of information on the etching of metal borides, mostly confined to theoretical studies. The MBenes are predicted to be both outstanding HER catalysts and excellent electrodes for lithium batteries.[36] To date, moderate progress has been made in etching aluminum out of both MoAlB [37] and Cr_2AlB_2 [38] phases, however delamination has not been demonstrated.

Chapter 2 reports on the synthesis, crystal chemistry, electronic structure and chemical bonding analysis of a new high temperature

modification of NbOsB adopting a new structure type in which isolated B and infinite zigzag B chains exist. This combination has only been found in the o-Ni_4B_{3-x} and the recently discovered $Ru_9Al_3B_8$ structures.[39–41] Single crystal X-ray diffraction data shows a partial osmium substitution onto all of the niobium sites, which is subsequently rationalized through structural and electronic effects. Density functional theory (DFT) was used to support the finding that local stabilization of the infinite boron chain fragment was favored over a global destabilization of the structure. It is suggested that a small pseudogap would allow for a change in the valence electron count, and a smaller atom may help relieve stress on the niobium sites.

In chapter 3, synthesis methods and data are presented on the etching of aluminum from the M_2AlB_2 (M=Cr, Mn, Fe) structure, and the exfoliation of the leftover MB layers. A combination of powder X-ray diffraction(XRD), scanning and tunneling electron microscopy (SEM/TEM), atomic force microscopy (AFM), energy dispersive X-ray spectroscopy (EDX/EDS), and bader charge analysis computed using the Vienna ab-initio software package (VASP) were used to support the 2D nature and behavior of the samples. A future work section outlines potential next steps for this avenue of research, including necessary

surface characterization and applying this method towards designing battery electrodes.

Chapter 2: HT-NbOsB: Experimental and Theoretical Investigations of a New Boride Structure Type Containing Boron Chains and Isolated Boron Atoms

Introduction

The original goal of this work was a continuation of "Peierls-Distorted Ru-Chains and Boron Dumbbells in Nb_2RuB_2 and Ta_2RuB_2 from First-Principles Calculations and Experiments". [42] Touzani *et. al.* predicted, using USPEX evolutionary algorithm,[43–45] that Nb_2RuB_2 and Ta_2RuB_2 could potentially crystallize in the Mn_2AlB_2 structure type. This was interesting at the time because the Mo_2FeB_2 and Nb_2OsB_2 structure types, the latter being a two-fold superstructure of the former, were known and ruthenium is isoelectronic to osmium. Eventually Nb_2RuB_2 was found to crystallize in the expected Nb_2OsB_2 structure, but the question lingered concerning the other predicted structure. An attempt was made to synthesize the inverse metal composition, $NbRu_2B_2$, in the Mn_2AlB_2 structure, thinking that the relative electropositivities of the metals may affect which structure is obtained. This proved unsuccessful, so the same reasoning was applied to $NbOs_2B_2$, which was the starting composition in this study. Although the sought after Mn_2AlB_2 structure was not obtained, it is

interesting to note that both the structure reported here and the Mn_2AlB_2 structure contain infinite zig zag boron chains.

Results and Discussion

Phase analysis

The $Nb_{1-x}Os_{1+x}B$ phase was synthesized using a 1:2:2 (Nb:Os:B) ratio for the starting pellet. This produced 62.4(9) wt% of the $Nb_{1-x}Os_{1+x}B$ (*Pnma, no. 62*) phase, obtained from the Rietveld refinement of the powder data. It was observed that the side product (elemental osmium) had slightly larger lattice parameters than the literature values, which suggests interstitial atom (boron) or substitution with the larger Nb, or both. The data and lattice parameters from this refinement are summarized in **Table S2.1** and **Figure S2.2** of the supporting information (SI). The refinement model is in close agreement with the single crystal refinement below (**Table 2.1**). EDX of a single crystal confirmed the metal ratio, which showed a Nb:Os ratio of 2.5:3.3 (**Figure S2.3**), which is in good agreement with the single crystal refinement considering the rough surface of the crystal.

Table 2.1 *Single crystal refinement parameters of* $Nb_{0.83}Os_{1.17}B$.

Formula weight (g/mol)	310.17
F (000)	127.7
Crystal size (mm)	0.03 x 0.02 x 0.10
θ range (°)	3.159 ≤ θ ≤ 33.794
hkl range	-17 ≤ h ≤ 16
	-4 ≤ k ≤ 4
	-19 ≤ l ≤19
Reflections Independent reflections	4692 991
Number of parameters refined	49
Space group; Z	*Pnma* (no. 62), 12
a (Å)	11.283(2)
b (Å)	3.0101(4)
c (Å)	12.883(2)
V (Å^3)	437.54(5)
Calculated density (g cm^{-3})	14.105
Absorption correction	Numerical
Absorption coefficient *μ* (mm^{-1})	8.84
GooF	1.118
*R*1; *wR*2	0.0441; 0.0938
Difference peak/hole (e Å^{-3})	5.02/-4.92
ICSD entry no.	433752

Structure Refinement and Crystal Chemistry

The final structure refinement of the single-crystal data in the orthorhombic space group *Pnma* indicated that all niobium sites are partially occupied by osmium (niobium occupancies: 0.80(1), 0.80(1), 0.90(1), on three different sites). The mixed occupancies lead to a $Nb_{0.83}Os_{1.17}B$ stoichiometry which can be generalized by the formula $Nb_{1-x}Os_{1+x}B$, where the maximal amount of osmium x = 0.17 at the niobium sites has probably been reached because an excess of osmium was used during the synthesis. The mix-occupancies were also found in the powder data [Nb: 0.82(3), 0.79(3), 0.87(3)] and agreed well with those from the single-crystal data.

This new structure type is composed of two main subunits (**Figure 2.1**), the first being the infinite boron chain extending into the *b* direction. This chain is contained within face sharing niobium prisms, each of which shares two of its three faces. All three niobium sites reside in fully capped pentagonal prisms (**Figure 2.2**) which have the large pentagonal face perpendicular to the *b* direction. In addition, osmium atoms partially occupy all niobium sites. The other subunit is composed of osmium trigonal prisms, all of which contain a boron atom. These trigonal prisms are bound to adjacent osmium prisms at two of their three corners; the third is corner sharing with a mixed

trigonal prism, which serves as a link between the two subunits. This mixed trigonal prism is corner sharing with both the osmium trigonal prisms and the niobium trigonal prisms. Because the niobium and osmium prisms are perpendicular to each other, each Os-based slab is offset from the next by half of the length of the *b* direction.

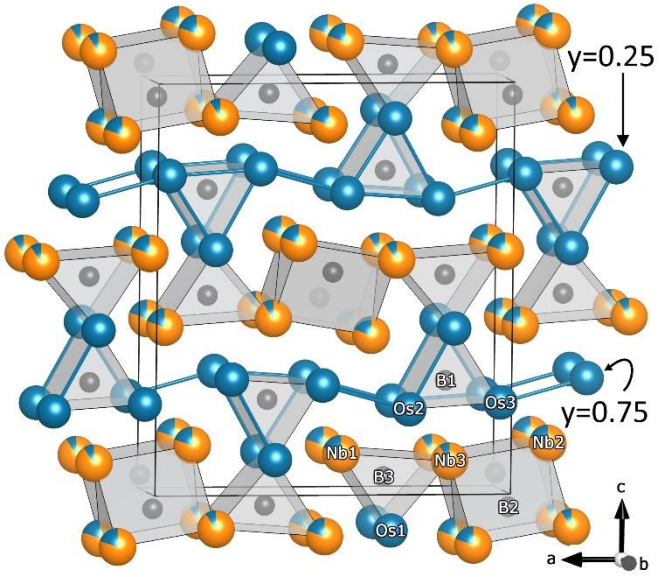

Figure 2.1 The extended structure of $Nb_{1-x}Os_{1+x}B$, projected down the *b* direction. Niobium and osmium atoms form boron-centered trigonal prisms, in perpendicular directions to each other. From this projection the osmium substructure is clear. Alternating Os-based slabs are offset in the *b* direction. Niobium atoms are shown in orange, osmium in blue, and boron in black.

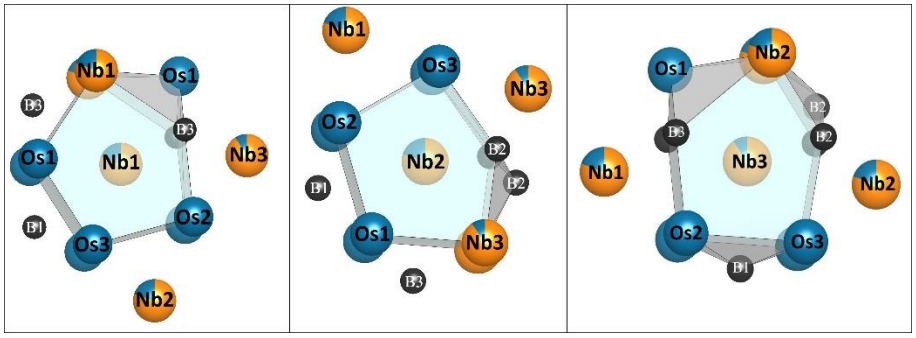

Figure 2.2 The coordination polyhedra around the three niobium positions. All polyhedra here are fully capped pentagonal prisms. Niobium atoms are shown in orange, osmium in blue, and boron in black.

The $Nb_{1-x}Os_{1+x}B$ structure (**Figure 2.1**) is strikingly similar to the orthorhombic Ni_4B_{3-x} structure (**Figure 2.3**, left), sharing the same *Pnma* space group and very similar lattice parameters [a = 11.9540(8), b = 2.9815(3), c = 6.5684(5) for Ni_4B_{3-x}]. [39] Both contain infinite boron chains perpendicular to the layer of boron-filled trigonal prisms. However, in the Ni_4B_{3-x} structure, the prisms containing the boron chains are corner sharing in one direction, whereas in the $Nb_{1-x}Os_{1+x}B$ structure they are separated by different trigonal prisms. This can be related to the M:B ratios, 2:1 vs 4:3, where the ratio with higher boron content (that of Ni_4B_{3-x} structure) leads to condensation of their prisms sharing and thus to more boron chain fragments. These metal trigonal prisms are also offset by half a length in the b direction, due to the staggering of the chain fragment. This new structure also shares many similarities to the recently

discovered NbRuB (*Pmma*)[46] and the $Ti_{1+x}Rh_{2-x+y}Ir_{3-y}B_3$ (*Pbam*, also adopted by the LT-NbOsB) [18] structure types (**Figure 2.3**, middle and right, respectively). These similarities include late transition metal (osmium, ruthenium) forming trigonal prisms which are connected via inter-prism bonds and contain isolated boron atoms. These prisms form puckered layers as shown in **Figures 2.1 and 2.3** (middle and right). The Os_6B prisms connections are very similar to those of the Ru_6B prisms in NbRuB. [46] However, in contrast to the NbRuB structure, the layers of Os_6B prisms in the $Nb_{1-x}Os_{1+x}B$ structure are offset by half a length in the *b* direction (compare **Figures 2.1 and 2.3 right**). The Os_6B prism offset is compensated by the niobium prisms, which are aligned perpendicularly and face sharing. This perpendicular arrangement of trigonal prisms is in contrast with the typical parallel alignment found in metal-rich borides.[5] In the NbRuB structure, the niobium and boron also form trigonal Nb_6B prisms, which are alternatingly face sharing and edge sharing along one direction, with B_2 dumbbell pairs forming in the face sharing trigonal prisms. However, in the new $Nb_{1-x}Os_{1+x}B$ structure, the Nb_6B prisms are always sharing two faces with each other forming chains in the *b* direction. This boron arrangement is extremely similar to the boron chain found in FeB.[12]

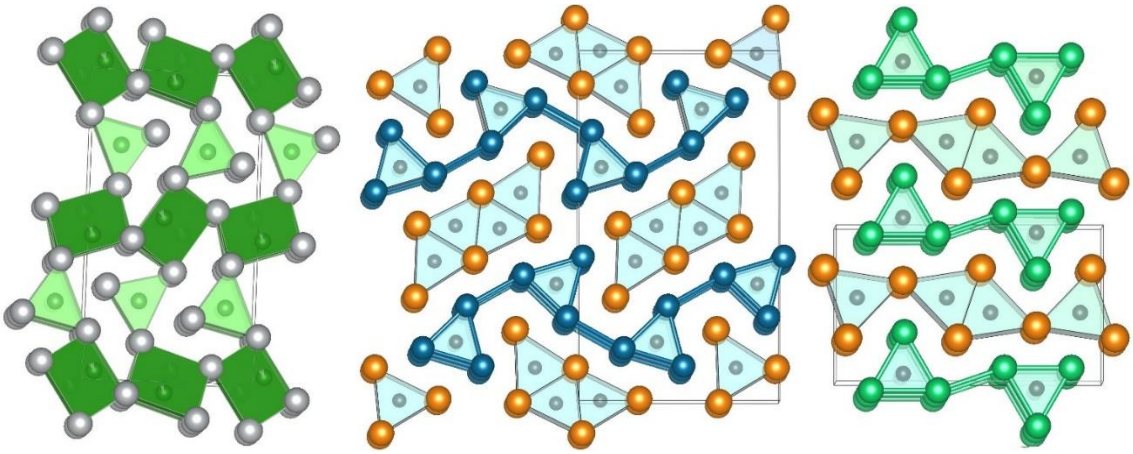

Figure 2.3 The Ni_4B_{3-x} (Left: *Pnma, no. 62*), NbOsB (Middle: *Pbam, no. 55, $Ti_{1+x}Rh_{2-x+y}Ir_{3-y}B_3$* type), and NbRuB (Right: *Pmma, no. 51*) structures are shown for comparison. Nickel atoms are shown in grey, boron in black inside the prisms, niobium in orange, osmium in blue, and ruthenium in bright green.

To check if the discrepancy in the partial osmium substitutions could be structurally driven, we have calculated the volumes of the three niobium prisms: V_{Nb1} = 38.6 Å^3, V_{Nb2} = 36.3 Å^3, and V_{Nb3} = 33.9 Å^3. The Nb-prism volume decreases from Nb1 to Nb2, and to Nb3. At first glance, it appears that Nb1 and Nb2 would be similar in volume, and they would if it were not for the rather large difference in one of the metal-boron bonds. The metallic bonds are of similar length, and so is one of the metal-boron bonds. However, the bond between Nb1 and B3 is 2.89 Å in the Nb1 polyhedron, whereas in the Nb2 polyhedron the B2-Nb3 bond is only 2.51 Å. Combining the decreasing volume for the three polyhedra with the fact that niobium is a larger metal than osmium, which would lead to the expectation of niobium being

preferentially on a larger site (Nb1), it becomes clear that the main driving force for Nb/Os substitution is not structural.

Something unusual for borides is the mixed trigonal Nb_4Os_2B prism around B3, with two niobium atoms and one osmium atom on each triangular face, which connect the face-sharing niobium FeB-like fragments to the extended osmium slabs. Similar mixed trigonal prisms can be found in the TiNiSi (*Pnma,* no. 62), $Ti_{1+x}Rh_{2-x+y}Ir_{3-y}B_3$, and NbCoB (*Pmnn*, no. 59) structure types, amongst others. The B1 coordination is in a similar environment, but the prism in this case is entirely osmium. Of note is that both prisms are fully capped. Both B1 and B3 coordinations are significantly different from B2, which makes up the boron chain. This chain has a bond angle of 116.2(8)^o, which is different from the ideal 120^o if the boron sat at the center of an equilateral prism. The boron sits in an off-centered position in all three polyhedra. This is due to the anisotropic coordination environments around these atoms. For the B2 infinite chain, the angle distortion is primarily due to the distortion of the niobium prisms in the FeB fragment. Compared to the ideal NbB structure [47], the Nb-Nb distance in the trigonal face of the prisms has been compressed roughly 10%, from 3.30 Å to 2.95 Å. At the same time, the Nb-Nb distance parallel to the boron chain has been compressed from 3.16 Å

to 3.01 Å. However, the aspect ratio for both structures is almost identical, at 0.96 for NbB, and 0.95 for the structure reported here. This compression also explains the shortened B-B bond distance, from 1.86 Å in NbB to 1.77 Å here. This bond length is on the shorter end of the typical range of B-B bonds, which falls between 1.7 and 1.9 Å[6], and is reasonable considering the atomic radius of boron is ~0.8 Å. Because the 3.01 Å Nb-Nb bond length in the *b* direction is linked to the height of the osmium trigonal prisms, there is a structural balance between compressing the niobium bonds and stretching the osmium bonds. Thus, the smaller osmium atom substituting onto the niobium sites may occur in part to relieve the strain resulting from this imbalance. Also, it may be possible that a larger atom on the osmium sites would relieve some of this stress and allow the niobium fragment to relax. Finally, the angle Nb2-Nb3-Nb2 is not a perfect 90^{o}, but is actually 88.6^{o}, meaning the FeB fragment actually has a parallelogram cross-section. The niobium richer Nb3 site is pushed slightly further apart due to a larger average size, and the Nb2 sites are brought together, thus this distortion supports the mixed occupancy found in the single crystal refinement.

Chemical Bonding Analysis

Chemical bonding analysis was carried out by using the crystal orbital Hamilton population (COHP) approach.[48] These populations were integrated up to the Fermi energy to obtain a semi-quantitative value (ICOHP) which reflects the bond strength between a pair of atoms. Calculations are done on the $Nb_{1-x}Os_{1+x}B$ composition with x = 0. The ICOHP estimates the bond strength, where an increase in the negative ICOHP represents a stronger bond, and vice versa. In general, the trend in chemical bonding found for similar compounds (e.g. NbRuB and TaRuB): All boron-based interactions are the strongest (highest -ICOHP values) followed by the heterometallic metal-metal bonds and the homometallic metal-metal bonds. This bonding pattern confirms the structural description based on boron-centered metal prisms and the presence of boron chains.

Table 2.2 *List of nearest neighbor interactions in the crystal structure of NbOsB and their corresponding average -ICOHP values.*

Bond	d_{exp}, Å	Average -ICOHP, eV
Nb2-Os3	2.747(2)	1.008
Nb3-Os3	2.802(2)	0.792
Nb3-Os2	2.807(2)	0.786
Nb2-Os1	2.810(2)	0.844
Nb1-Os1	2.813(2)	0.862
Nb3-Os1	2.837(3)	0.763
Nb1-Os2	2.839(2)	0.909
Nb2-Os2	2.821(2)	0.880
Nb1-Os3	2.870(2)	0.866
Nb1-Os1	2.885(3)	0.679
Os1-Os3	2.759(2)	0.690
Os2-Os3	2.857(2)	0.815
Os1-Os2	2.881(2)	0.530
Os2-Os3	2.894(2)	0.476
Os2-Os2	3.010(1)	0.521
Os3-Os3	3.010(1)	0.494
Os1-Os1	3.010(1)	0.414
Nb2-Nb3	2.949(2)	0.592
Nb1-Nb1	2.977(3)	0.660
Nb1-Nb1	3.010(1)	0.625
Nb2-Nb2	3.010(1)	0.572
Nb3-Nb3	3.010(1)	0.531
Nb2-Nb3	3.158(3)	0.792

Bond	Dexp, Å	Average -ICOHP, eV
B2-B2	1.77(3)	3.648
Os1-B3	2.16(2)	1.716
Os3-B1	2.19(2)	1.665
Os2-B1	2.20(2)	1.627
Os1-B1	2.31(2)	1.254
Os2-B3	2.38(3)	1.057
Os3-B2	2.51(3)	0.680
Nb2-B2	2.29(3)	1.141
Nb2-B2	2.33(3)	0.936
Nb3-B2	2.36(3)	1.016
Nb1-B3	2.38(2)	1.097
Nb3-B3	2.43(3)	0.968
Nb3-B1	2.54(3)	0.702

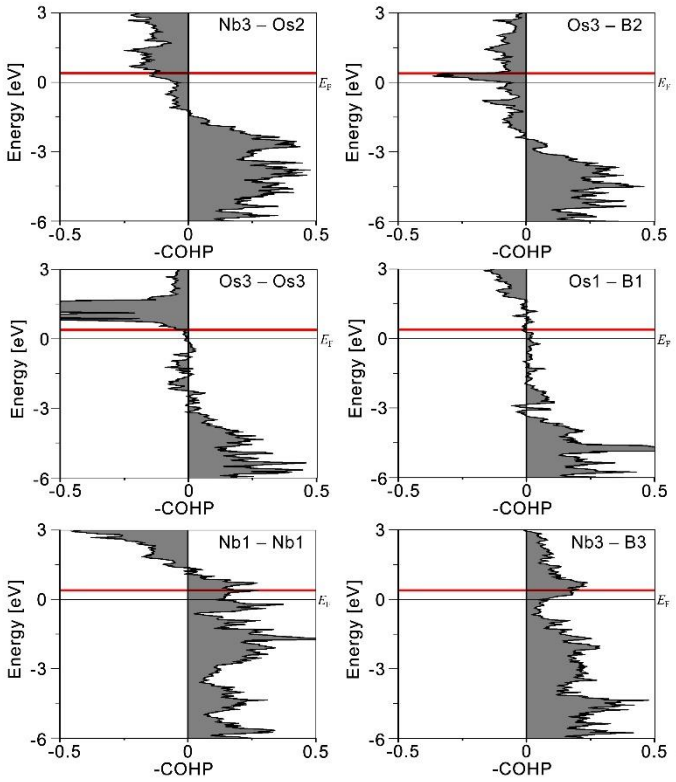

Figure 2.4. COHP plots for selected bonds in stoichiometric NbOsB. Negative COHP values represent bonding states for a given energy level. The fermi energy (E_F) is set to 0. The top two plots show bonds which were strongly destabilized, while the middle two show bonds which were mildly affected, and the bottom show strongly stabilized bonds. The red line shows the Fermi energy shift of the experimental, non-stoichiometric compound.

We have evaluated the effects of the osmium substitution on the Nb-sites by shifting the Fermi energy (E_F) of the ideal composition relative to the band structure according to the rigid band model (see gray and red lines in **Figures 2.4, 2.5 and 2.6**, where the gray line represents the ideal E_F while the red line represents E_F of the experimental composition). COHP plots for some representative bonds are shown in

Figure 2.4. The COHP plots suggest that Nb-Nb and Nb-B interactions still have bonding states above the Fermi level which can be filled with additional electrons (**Figure 2.4**, bottom). In contrast, Os-Nb and Os-B interactions are forced to populate antibonding states (**Figure 2.4**, top). Neither Os-Os bonds nor the B2-B2 chain are significantly impacted. In particular, the face sharing niobium trigonal prisms benefit immensely from the osmium substitution **(Figure 2.5**, right**)**. This suggests that the substitution results in strongly stabilized Nb-Nb interactions, despite a small overall destabilizing effect as shown by the red line being placed in a slightly antibonding region in the combined COHP plot of all interactions (**Figure 2.5**, left). Interestingly, the site with the least substitution is also the site with the smallest coordination environment, even though osmium is a smaller atom than niobium. This is the opposite of what would be expected from size arguments and it suggests the driving force is not geometrical. The Nb3 site is the only metal site that is coordinated to both the infinite boron chain and isolated boron atoms. By examining this site in the context of boron rich borides, the higher niobium occupancy makes sense, because boron rich phases are typically formed with earlier transition metals due to their relatively higher electropositivity.[33] Accordingly, the Nb3 site prefers more Nb and less Os than the other

two Nb sites. Looking at the total density of states (DOS) plot (**Figure 2.6**), there is a deep pseudo-gap near the Fermi level. This window allows the Fermi level to be shifted without a significant impact on the stability, which in turn is what allows the partial osmium substitution to occur. At x = 0, Fermi falls in a minimum, indicating that the stoichiometric composition is electronically stable. At x = 0.17 (experimental composition), the new Fermi level (red line in the DOS) still falls within the pseudo-gap range, but clearly on the edge and thus in a slightly less stable position. This is reflected by the small negative total COHP peak above the Fermi energy. All of this supports the notion that this structure is greatly flexible on the Nb3 site, which could also adopt a more electropositive atom such as titanium due to both the smaller size and the presence of the deepest minimum just below E_F. Alternatively, a group 6 metal such as molybdenum may also be able to relieve structural strain while supplying the electrons gained from the osmium substitution. Since there are two forces both contributing to the current mixed occupancies, it is important to try both to determine if one is dominant over the other. It is possible that relieving the structural strain also decreases the need for more niobium bonding states to be populated, or that supplying electrons from elsewhere removes the need for substitution.

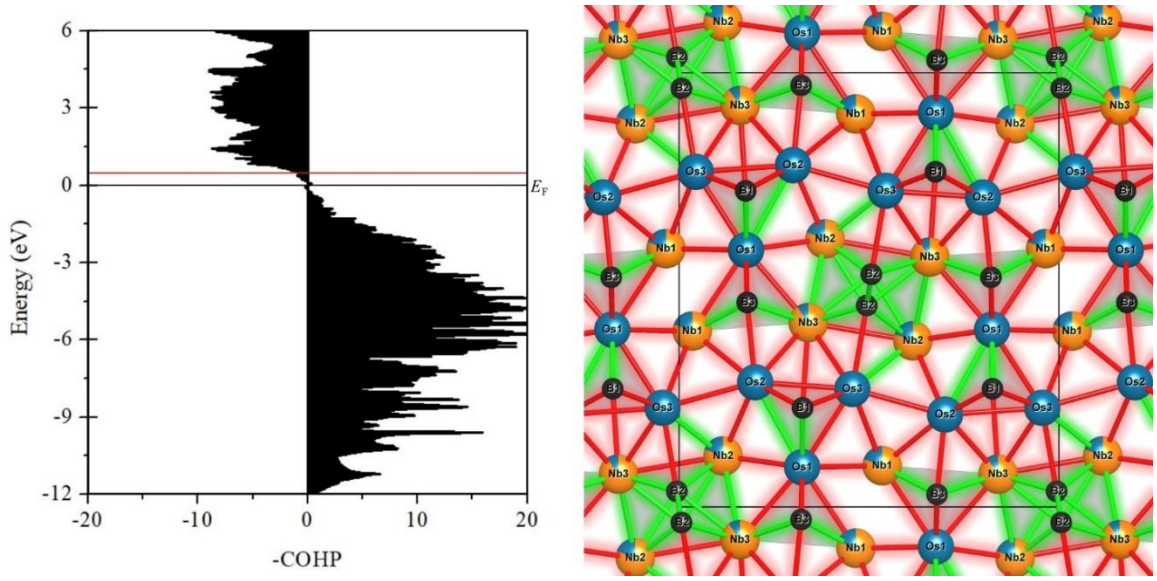

Figure 2.5 *Left*: Total COHP for the entire structure. Note the region directly adjacent to the Fermi energy, where there is a stability window before populating large numbers of antibonding states. The osmium substitution shifts the Fermi and fills additional bonding states. *Right*: Representative figure with stabilized bonds shown in green and destabilized bonds in red.

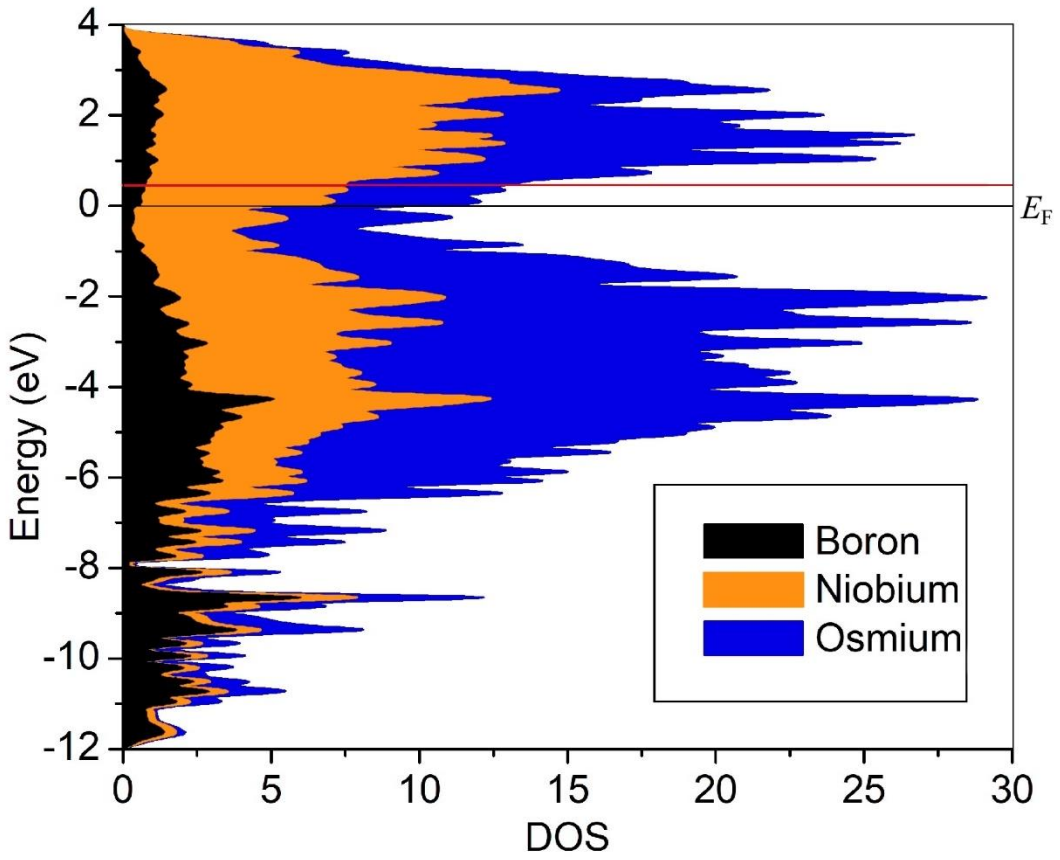

Figure 2.6 Density of states for NbOsB structure and projected DOS for Nb and Os. The fermi energy (E_F) is set to zero.

It was recently found experimentally that LT-TaRuB [49] crystallizes with $Ti_{1-x}Rh_{2+x-y}Ir_{3-y}B_3$ [18] structure type while HT-TaRuB [19] adopts the NbRuB [46] structure type. Because another modification of NbOsB was recently reported to crystallize with the $Ti_{1-x}Rh_{2+x-y}Ir_{3-y}B_3$ structure type, it is interesting to find out the thermodynamic stability relative to the new modification as well as the NbRuB structure type. DFT calculations were thus performed to determine the total energies of

these related structure types, so that a comparison could be made. These calculations suggest that the $Ti_{1-x}Rh_{2+x+y}Ir_{3-y}B_3$ structure type is the most stable at 0 K by 3.2 kJ/mol per formula unit, thus the already known NbOsB is the low-temperature modification. However, the new NbOsB is more stable than the NbRuB-type structure by 5.7 kJ/mol per formula unit. This trend is in line with prior calculations for the Ta-Ru-B phase space[49], and suggests that the new phase is a high temperature modification of NbOsB ($Ti_{1-x}Rh_{2+x-y}Ir_{3-y}B_3$-type).

Conclusion

A new ternary boride structure has been discovered, with a unique combination of structural motifs common to other borides with higher and lower M:B ratios. Both infinite boron chains (FeB fragment) and isolated boron atoms within trigonal prisms (Re_3B fragment) are present. Single crystal XRD confirms partial substitution of osmium onto the niobium sites, indicating that the stoichiometric structure is electron deficient. DFT and COHP analysis were performed to show unfilled bonding states in the theoretical stoichiometric NbOsB phase, which was combined with structural analysis to explain the partial substitution of osmium onto the niobium sites. It was observed that a small number of Nb-Nb and Nb-B bonds were highly stabilized at the cost of a large number of slightly unfavorable Os-Nb and Os-B

interactions. This localized stabilization compensates for the highly compressed FeB fragment. It is predicted that a group 6 metal would be more appropriate for the niobium site, and that a larger metal on the osmium site may help relieve internal strain between the osmium and niobium substructures.

Experimental Section

Synthesis and Characterization: The $Nb_{1-x}Os_{1+x}B$ compound was prepared from elemental powders of niobium (>99.8%, Alfa Aesar), osmium (>99.9%, Arcos Organics), and boron (amorphous & crystalline, >99%, Alfa Aesar). The powders were ground and mixed in a 1:2:2 ratio, respectively, then pressed into pellets. The pellets were then arc-melted in a water-cooled copper crucible under argon atmosphere, using a tungsten electrode and 40 A of current. The argon was purified by passage through silica gel, molecular sieves, and titanium sponge (950 K). The pellet was rotated in the crucible a couple of times and remelted during the arc procedure to ensure homogeneity. Weight losses during the melting process were negligible. The final product from each synthesis was a metal bead, which was then crushed to obtain powder and single crystals for further analysis.

Phase analysis was performed by X-ray powder diffraction at room temperature with a Rigaku MiniFlex 600, using a Cu Kα radiation source (λ=1.5418 Å). Rietveld refinement (full-matrix least-squares refinement) was performed using the FULLPROF program[50]. Energy-dispersive X-ray spectroscopy (EDX) was used on single crystals to verify the metal ratio (**Figure S2.3**). An attempt was made to improve the yield by starting with a 1:1:1 composition, but this led mainly to the Nb_2OsB_2 phase suggesting an incongruently melting behavior for the new compound.

Crystal Structure Determination: The single crystals were isolated using an optical microscope and were affixed to a glass capillary for X-ray diffraction with a Rigaku XtaLAB mini. The crystallographic data are summarized in **Table S2.4** below. The structure was solved using direct *ab-initio* methods, and refined using the SHELX programs (full-matrix least-squares based on F^2).[51,52] The metal atoms were refined using anisotropic thermal displacement parameters, and the boron atoms were refined isotropically. Numerical absorption correction based on the crystal geometry were applied.[53]

Computational Methods: The Vienna Ab-initio Simulation Package (VASP) [54] was used to perform *ab-initio* DFT calculations for structural optimization via the projector augmented wave (PAW)

method [55]. Exchange and correlations were treated with the generalized gradient approximation (GGA) functional as parameterized by Perdew, Burke, and Ernzerhof [56] with an energy cut-off of 500 eV. For structural relaxation, a convergence threshold of 0.01 eV/Å was used. The lattice parameters increased by ~1% during this relaxation, consistent with the expectations for GGA.

Electronic calculations were done using the linear muffin-tin orbitals approximation (LMTO) as implemented in TB-LMTO 4.7.[57] Exchange and correlation were treated with the LDA functional by Kohn and Sham[58]. A k-mesh of 6 x 24 x 6 was used, which gives 208 k-points in the irreducible Brillouin zone. No empty spheres were needed to achieve 100% filling of the unit cell. The basis sets include: 5s, 5p, 4d, and 4f for niobium; 5s, 5p, 6d, and 6f for osmium; 2s, 2p, and 3d for boron. The f orbitals for osmium and niobium and the d orbital for boron were treated by the Löwdin downfolding technique.[59]

References

1 M.T. Yeung, R. Mohammadi, R.B. Kaner, *Annu. Rev. Mater. Res.*, 2016, **46**, 465–485.

2 J. Nagamatsu, N. Nakagawa, T. Muranaka, Y. Zenitani, J. Akimitsu, *Nature*, 2001, **410**, 63–64.

3 H. Park, A. Encinas, J.P. Scheifers, Y. Zhang, B.P.T. Fokwa, *Angew. Chemie - Int. Ed.*, 2017, **56**, 5575–5578.

4 B.P.T. Fokwa, *Eur. J. Inorg. Chem.*, 2010, **2010**, 3075–3092.

5 J.P. Scheifers, Y. Zhang, B.P.T. Fokwa, *Acc. Chem. Res.*, 2017, **50**, 2317–2325.

6 B. Albert, H. Hillebrecht, *Angew. Chemie - Int. Ed.*, 2009, **48**, 8640–8668.

7 T. Mori, *J. Phys. Conf. Ser.*, 2009, **176**, 012036.

8 G. Akopov, M.T. Yeung, R.B. Kaner, *Adv. Mater.*, 2017, 1604506.

9 P. Villars, L.D. Calvert, 『Person's Handbook of Crystallographic Data for Intermetallic Phases』, CD-ROM ed., ASM International, Materials Park OH, 1991.

10 Y.P. Kuz'ma, Yu.B.; Yarmolyuk, *Zhurnal Strukt. Khimii*, 1971, **12**, 458.

11 M. Ade, D. Kotzott, H. Hillebrecht, *J. Solid State Chem.*, 2010, **183**, 1790–1797.

12 T. Lundstrom, *Pure Appl. Chem.*, 1985, **57**, 1383–1390.

13 T. Mori, H. Borrmann, S. Okada, K. Kudou, A. Leithe-Jasper, U. Burkhardt, Y. Grin, *Phys. Rev. B*, 2007, **76**, 064404.

14 J. Bauer, J.-F. Halet, J.-Y. Saillard, *Coord. Chem. Rev.*, 1998, **178–180**, 723–753.

15 T. Mori, *Handb. Phys. Chem. Rare Earths*, 2007, **38**, 105–173.

16 P.I. Chepiga, M.V.; Kuzma, Yu.B.; Kripyakevich, *Dopovidi Akad. Nauk Ukr. RSR, Seriya A Fiz. Ta Mat. Nauk.*, 1972, 856–858.

17 B.P.T. Fokwa, M. Hermus, *Angew. Chemie Int. Ed.*, 2012, **124**, 1734–1737.

18 C. Goerens, B.P.T. Fokwa, *J. Solid State Chem.*, 2012, **192**, 113–

119.

19 Q. Zheng, R. Gumeniuk, H. Rosner, W. Schnelle, Y. Prots, U. Burkhardt, Y. Grin, A. Leithe-Jasper, *J. Phys. Condens. Matter*, 2015, **27**, 415701.

20 M. Ade, H. Hillebrecht, *Inorg. Chem.*, 2015, **54**, 6122–6135.

21 J. Lu, S. Kota, M.W. Barsoum, L. Hultman, *Mater. Res. Lett.*, 2017, **5**, 235–241.

22 Y. Zhou, H. Xiang, F.Z. Dai, Z. Feng, *Mater. Res. Lett.*, 2017, **5**, 440–448.

23 M. Naguib, M. Kurtoglu, V. Presser, J. Lu, J. Niu, M. Heon, L. Hultman, Y. Gogotsi, M.W. Barsoum, *Adv. Mater.*, 2011, **23**, 4248–4253.

24 V.M. Hong Ng, H. Huang, K. Zhou, P.S. Lee, W. Que, J.Z. Xu, L.B. Kong, *J. Mater. Chem. A*, 2017, **5**, 3039–3068.

25 K. Maleski, V.N. Mochalin, Y. Gogotsi, *Chem. Mater.*, 2017, **29**, 1632–1640.

26 B. Anasori, M.R. Lukatskaya, Y. Gogotsi, *Nat. Rev. Mater.*, 2017, **2**, 16098.

27 M. Khazaei, A. Ranjbar, M. Arai, T. Sasaki, S. Yunoki, *J. Mater. Chem. C*, 2017, **5**, 2488–2503.

28 T. Ouisse, M.W. Barsoum, *Mater. Res. Lett.*, 2017, **5**, 365–378.

29 M.R. Lukatskaya, S. Kota, Z. Lin, M.-Q. Zhao, N. Shpigel, M.D. Levi, J. Halim, P.-L. Taberna, M.W. Barsoum, P. Simon, Y. Gogotsi, *Nat. Energy*, 2017, **6**, 17105.

30 Z.W. Seh, K.D. Fredrickson, B. Anasori, J. Kibsgaard, A.L. Strickler, M.R. Lukatskaya, Y. Gogotsi, T.F. Jaramillo, A. Vojvodic, *ACS Energy Lett.*, 2016, **1**, 589–594.

31 X. Zhang, Z. Zhang, J. Li, X. Zhao, D. Wu, Z. Zhou, *J. Mater. Chem. A*, 2017, **5**, 12899–12903.

32 R. Li, L. Zhang, L. Shi, P. Wang, *ACS Nano*, 2017, **11**, 3752–3759.

33 B.P.T. Fokwa, *Encycl. Inorg. Bioinorg. Chem.*, 2014, 1–14.

34 R. Barua, B.T. Lejeune, L. Ke, G. Hadjipanayis, E.M. Levin, R.W. McCallum, M.J. Kramer, L.H. Lewis, *J. Alloys Compd.*, 2018, **745**, 505–512.

35 A.L. James, K. Jasuja, *RSC Adv.*, 2017, **7**, 1905–1914.

36 Z. Guo, J. Zhou, Z. Sun, *J. Mater. Chem. A*, 2017,.

37 L.T. Alameda, C.F. Holder, J.L. Fenton, R.E. Schaak, *Chem. Mater.*, 2017, **29**, 8953–8957.

38 H. Zhang, H. Xiang, F. zhi Dai, Z. Zhang, Y. Zhou, *J. Mater. Sci. Technol.*, 2018,.

39 S. Rundqvist, S. Pramatus, B. Lamm, A. Haug, H. Theorell, R. Blinc, S. Paušak, L. Ehrenberg, J. Dumanović, *Acta Chem. Scand.*, 1967, **21**, 191–194.

40 Z. Malik, A. Grytsiv, P. Rogl, G. Giester, J. Bursik, *J. Solid State Chem.*, 2013, **198**, 150–161.

41 S. Hirt, F. Hilfinger, H. Hillebrecht, *Zeitschrift Für Krist. - Cryst. Mater.*, 2018, **6**, 1–14.

42 R. St. Touzani, M. Mbarki, X. Chen, B.P.T. Fokwa, *Eur. J. Inorg. Chem.*, 2016, **2016**, 4104–4110.

43 A.R. Oganov, A.O. Lyakhov, M. Valle, *Acc. Chem. Res.*, 2011, **44**, 227–237.

44 A.O. Lyakhov, A.R. Oganov, H.T. Stokes, Q. Zhu, *Comput. Phys. Commun.*, 2013, **184**, 1172–1182.

45 A.R. Oganov, C.W. Glass, *J. Chem. Phys.*, 2006, **124**, 244704.

46 M. Mbarki, R. St. Touzani, B.P.T. Fokwa, *Eur. J. Inorg. Chem.*, 2014, **2014**, 1381–1388.

47 O. Schob, E. Parthé, *Acta Crystallogr.*, 1965, **19**, 214–224.

48 R. Dronskowski, P.E. Bloechl, *J. Phys. Chem.*, 1993, **97**, 8617–8624.

49 M. Mbarki, R.S. Touzani, C.W.G. Rehorn, F.C. Gladisch, B.P.T. Fokwa, *J. Solid State Chem.*, 2016, **242**, 28–33.

50 J. Rodriguez-Carvajal, FULLPROF 2000: A Rietveld Refinement and Pattern Matching Analysis Program, 2008.

51 G.M. Sheldrick, *Acta Crystallogr. Sect. A Found. Crystallogr.*, 2007, **64**, 112–122.

52 G.M. Sheldrick, *Acta Crystallogr. Sect. C Struct. Chem.*, 2015, **71**, 3–8.

53 G.M. Sheldrick, 1996,.

54 G. Kresse, D. Joubert, *Phys. Rev. B*, 1999, **59**, 1758–1775.

55 P.E. Blöchl, *Phys. Rev. B*, 1994, **50**, 17953–17979.

56 J.P. Perdew, K. Burke, M. Ernzerhof, *Phys. Rev. Lett.*, 1996, **77**, 3865–3868.

57 R.W. Tank, O. Jepsen, *Cell*, 1998, 1–27.

58 W. Kohn, L.J. Sham, *Phys. Rev.*, 1965, **140**, 1133–1138.

59 P.-O. Lowdin, *J. Chem. Phys.*, 1951, **19**, 1396–1171.

60 W. Sun, S.A. Shah, Y. Chen, Z. Tan, H. Gao, T. Habib, M. Radovic, M.J. Green, n.d.,.

61 J. Wen, X. Zhang, H. Gao, *Phys. B Condens. Matter*, 2018, **537**, 155–161.

62 A.N. Kolmogorov, M. Calandra, S. Curtarolo, *Phys. Rev. B - Condens. Matter Mater. Phys.*, 2008, **78**, .

Chapter 3: Exfoliation and Characterization of Novel 2D MBenes from Bulk Borides

Experimental Methods

Synthesis:

Starting material was made using elemental powders of boron (Alfa Aesar, amorphous and crystalline, 98%), aluminum (Acros Organics, 99.7%), and one of chromium (Alfa Aesar, 99%), manganese (Alfa Aesar, 99.95%), or iron (Acros Organics, 99%). Powders were mixed in a 3:2:2 ratio (Al:M:B), pressed into a pellet, then sealed inside a quartz tube in an alumina crucible under vacuum. Excess aluminum has been demonstrated to shift equilibrium towards the ternary boride and an intermetallic side product, instead of mixed boride phases.[20,21] The tubes were heated to 900 ^{o}C, then cooled to 600 ^{o}C over five days before cooling to room temperature. In all cases the product obtained was the desired M_2AlB_2 phase as well as an intermetallic side product made of aluminum and the respective transition metal.

Several methods have been tested for etching of the aluminum layers, outlined below:

Basic solution with potassium hydroxide (KOH):

The initial etching was performed using a modified procedure from James et al.[37] After removing the side products using dilute HCl for 10 minutes, the powder was left in a 25% KOH solution for 24 hours to etch out the aluminum from the structure. The product was filtered using a Büchner funnel, which leaves a grey-black clay on the filter paper while a clear liquid passed through. The powder was then washed using several centrifuge steps to remove residual potassium and aluminum ions and neutralize the pH before drying at 60 ^{o}C overnight. Initially NaOH was used, but the sodium ions were found to be difficult to remove via washing.

Acidic solutions:

Various acidic solutions were used, including 6 M hydrochloric acid (HCl) with potassium chloride, 5.8 M acetic acid with sodium acetate, and iron (III) chloride with 2.5 M HCl. The powder was left in solution for 24 hours. The product was filtered using a Büchner funnel, then washed using several centrifuge steps before drying at 60 ^{o}C overnight.

Characterization:

Phase analysis was performed by X-ray powder diffraction at room temperature with a Rigaku MiniFlex 600, using a Cu Kα radiation source (λ=1.5418 Å). Rietveld refinement (full-matrix least-squares refinement) was performed using the FULLPROF program. Energy dispersive X-ray spectroscopy (EDX) was used both in a NovaNanoSEM 450 scanning electron microscope (SEM) and a Tecnai G2 Sphera (FEI) transmission electron microscope (TEM).

Atomic force microscopy (AFM) measurements were done using a VEECO Dimension 5000 Atomic Force Microscope, with Nanoscope III control software. This unit is inside a vibration/acoustic isolation chamber to minimize outside noise. For these measurements tapping mode was used to reducing the lateral shear forces between tip and sample, thus minimizing tip and sample damage. Amplitude was set to 20 nm, integral gain was 0.1, and proportional gain was 0.2. Samples were prepared by drop casting an ethanol solution with the dispersed sheets onto a silicon substrate.

Computational Methods:

The Vienna Ab-initio Simulation Package (VASP) as used to perform ab-initio DFT calculations for structural optimization via the projector

augmented wave (PAW) method.[28,29,46-51,54,55] Exchange and correlations were treated with the generalized gradient approximation (GGA) functional as parameterized by Perdew, Burke, and Ernzerhof [56] with an energy cut-off of 600 eV. For structural relaxation, a convergence threshold of 0.01 eV/Å was used.

Results

Figure 2 below shows XRD data collected on Fe_2AlB_2 samples after a quick HCl wash to remove the intermetallic side product, in this case $Al_{13}Fe_4$, as well as after 24 hours in a 25% NaOH solution. The simulated XRD patterns were generated using Diamond crystallographic software. The pattern on the left was generated using the parameters for the reported structure, and the one on the right was generated using the same .cif file, but with the aluminum atoms deleted and the b direction of the unit cell stretched from 11.03 to 13.80 angstroms.

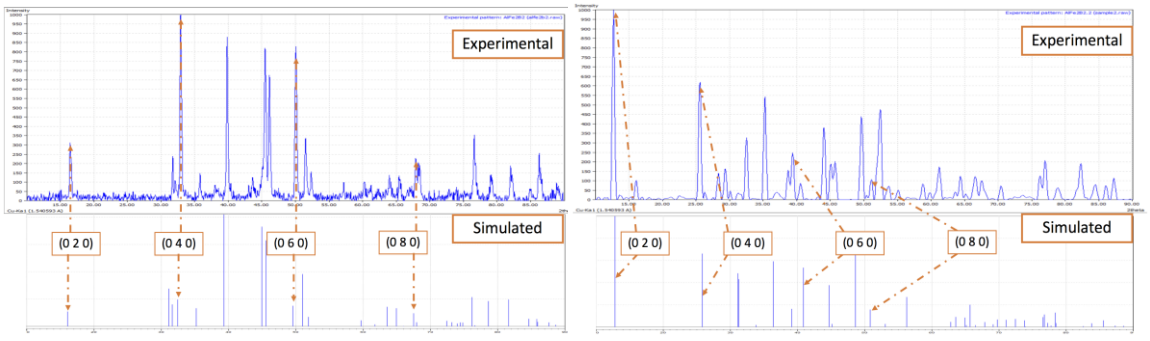

Figure 3.1 Powder XRD data of $AlFe_2B_2$ samples. a.) Sample after 10 minute HCl treatment to remove side products. b.) Sample after NaOH treatment for 24 hours. The shift in the (0 k 0) peaks to lower angles indicates an increase in the b direction

SEM images were collected for all three phases post etching. EDX demonstrates that for NaOH etching ~86% of the aluminum is removed from $AlMn_2B_2$ (**Figure S3.1**).

Figure 3.2 [Next Page] Top: Fe_2AlB_2 after 24 hours in 25% NaOH. The layering is very clear, and the etching appears to be periodic. Bottom: Mn_2AlB_2 after 24 hours in 25% NaOH. EDX data collected on this sample shows 20.4% manganese, 1.1% aluminum, which reflects ~90% aluminum removal.

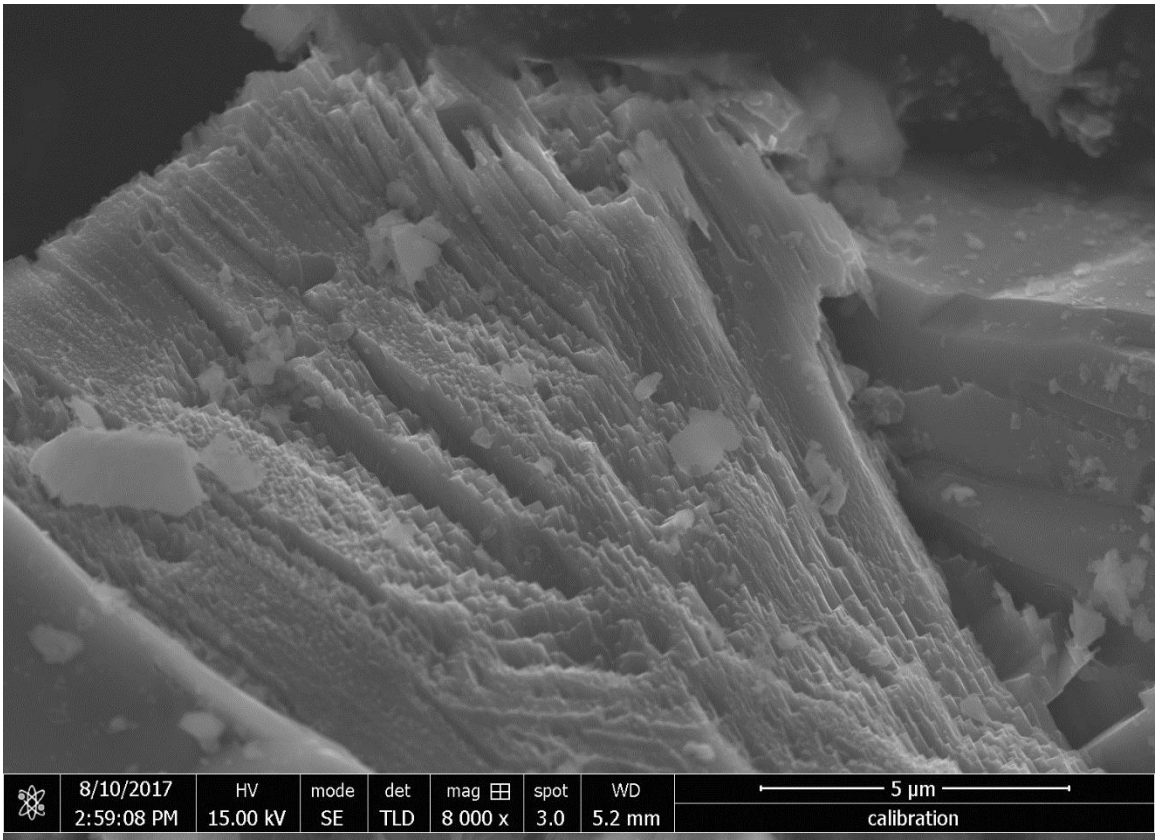
8/10/2017
2:59:08 PM
HV
15.00 kV
mode
SE
det
TLD
mag
8 000 x
spot
3.0
WD
5.2 mm
5 µm
calibration

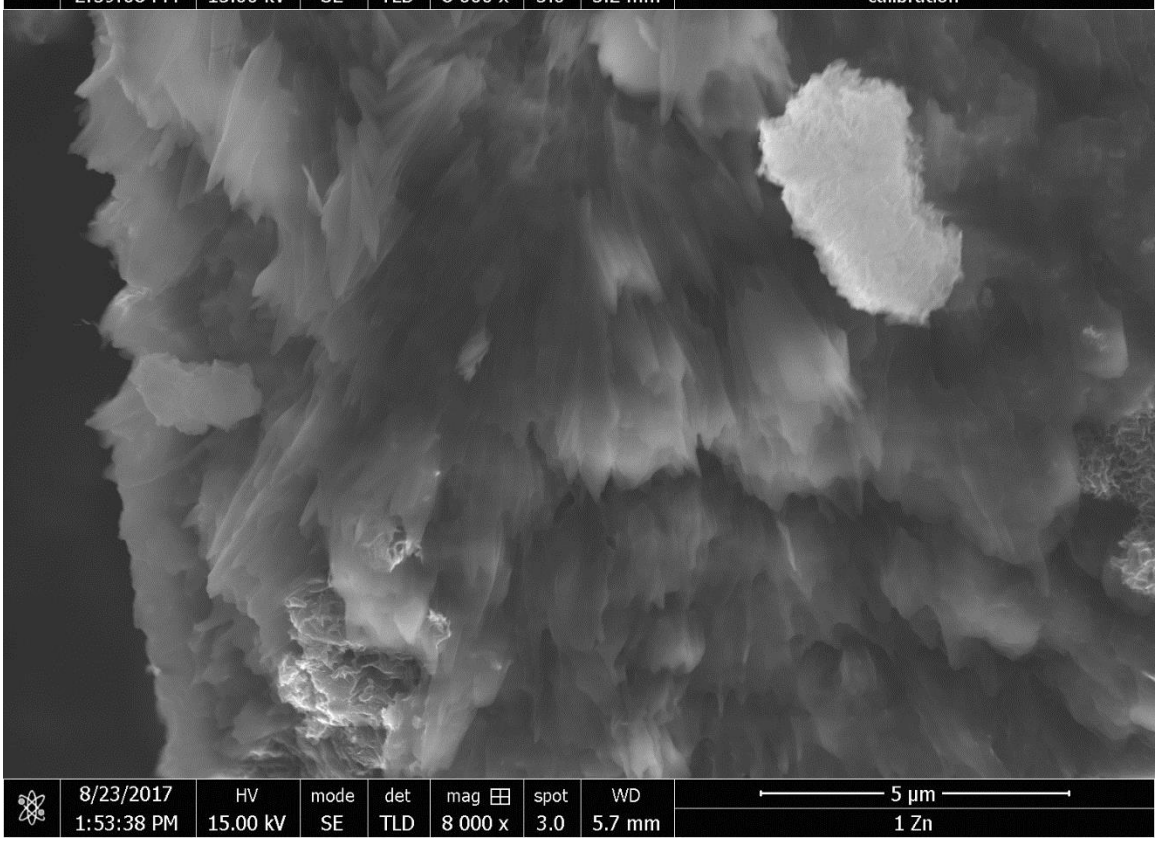
8/23/2017
1:53:38 PM
HV
15.00 kV
mode
SE
det
TLD
mag
8 000 x
spot
3.0
WD
5.7 mm
5 µm
1 Zn

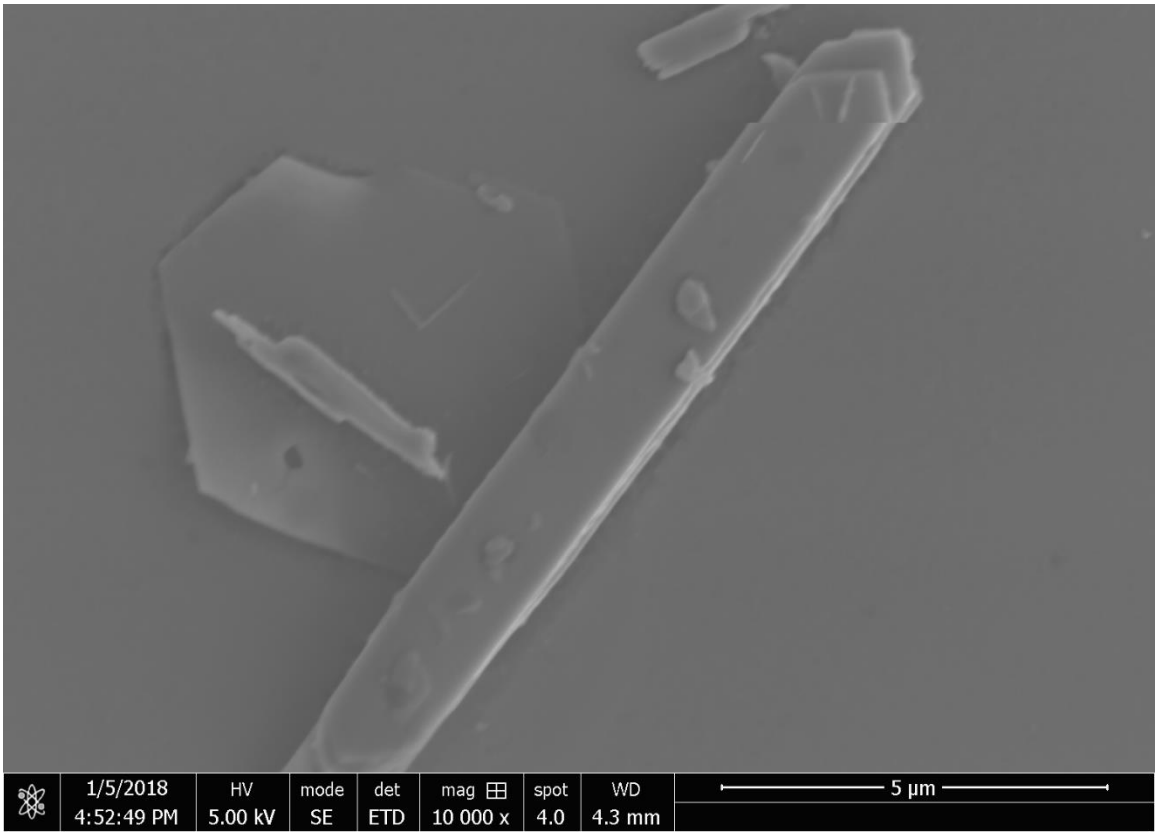

Figure 3.3 Cr_2AlB_2 etched for 24 hours in 25% KOH, drop cast from ethanol solution onto silicon substrate.

Bader charge analysis was done on all three phases with fully occupied aluminum sites, as well as 50% occupied and fully vacant aluminum sites. The charge reversal for the $Cr_2Al_0B_2$ structure is thought to be an artifact which reflects the instability of the MB layer without a charge compensating surface group.

Table 3.1 *Summary of Bader charge analysis results. Positive partial charges indicate that the atom is donating electrons and negative charge indicates that the atom is accepting electrons.*

Cr2AlB2	
Al=100%	Partial charge
Cr	**+0.35**
Al	**+1.5**
B	**-1.1**
Al=50%	
Cr	**+0.37/+0.75**
Al	**+1.5**
B	**-1.1/-0.7**
Al=0%	
Cr	**-0.65/0.69**
B	**+0.67**

Mn2AlB2	
Al=100%	Partial charge
Mn	**0**
Al	**+1.7**
B	**-0.85**
Al=50%	
Mn	**+0/+0.55**
Al	**+1.67**
B	**-0.87/-0.53**
Al=0%	
Mn	**+0.45**
B	**-0.55**

Fe2AlB2	
Al=100%	Partial charge
Fe	**-0.18**
Al	**+1.7**
B	**-0.67**
Al=50%	
Fe	**-0.15/+0.4**
Al	**+1.69**
B	**-0.71/-0.38**
Al=0%	
Fe	**+0.4**
B	**-0.39**

AFM measurements were made to determine the thickness of the exfoliated sheets. Images were processed using Gwyddion SPM data analysis software. In all cases the layers are approximately 2.5 nm thick and 1 μm in diameter, which corresponds to 4-6 layers. Thicker particulate roughly 0.2 μm in diameter and 20-40 nm thick was also present, both on the substrate and on the sheets.

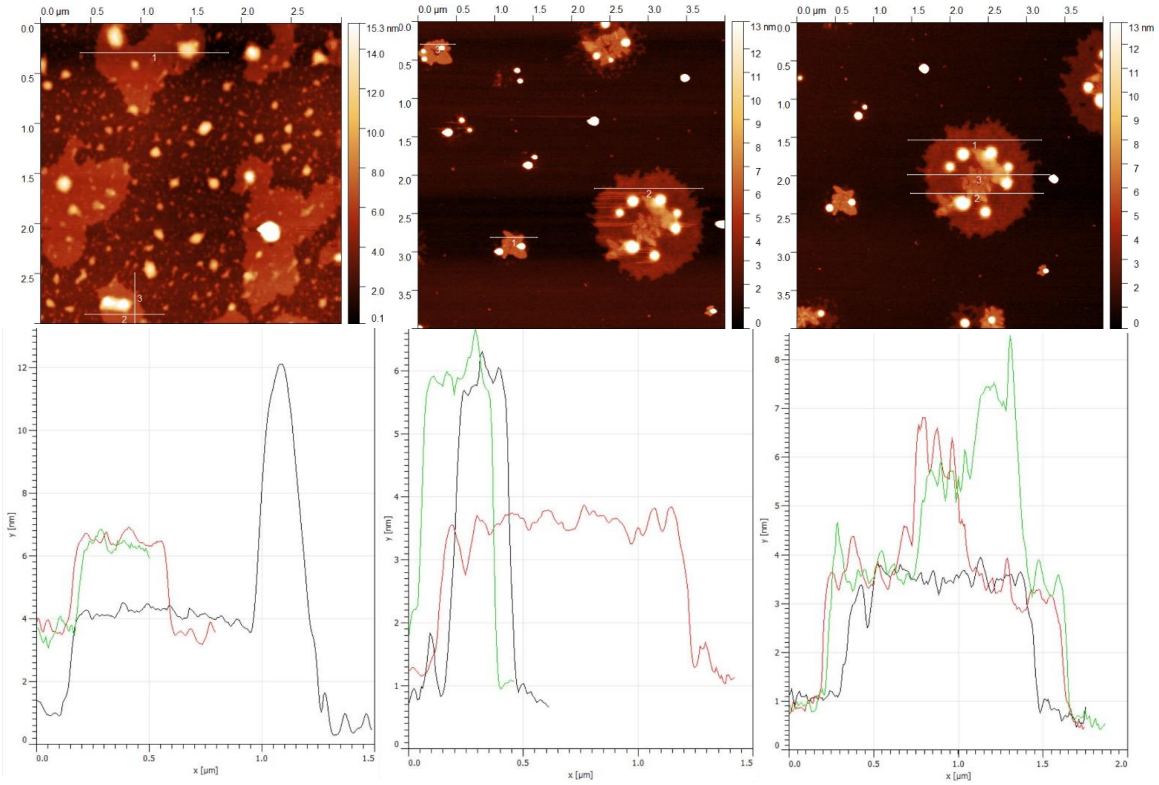

Figure 3.4 AFM images (top) and respective line profiles (bottom). In all cases, the labeling is 1=black, 2=red, 3=green. Left: Cr_2AlB_2 etched sample. Middle and right: Fe_2AlB_2 etched sample, post centrifuging.

TEM was used to determine the crystallinity of the resulting sheets and to perform local EDX measurements. **Figure 3.5** below shows a TEM image and diffraction pattern for an etched Cr_2AlB_2 sample. Individual layers are visible in the image, and the diffraction pattern shows that the sample is highly crystalline. **Figure S3.2** shows a higher magnification, and the entire image is of a single grain. Also in the supporting information are images of both manganese and iron samples, which are polycrystalline but show clear diffraction peaks (**Figure S3.3**). There is also a figure showing smaller particles from

Mn_2AlB_2, which have a needle or rod morphology and are aluminum rich (**Figure S3.4**).

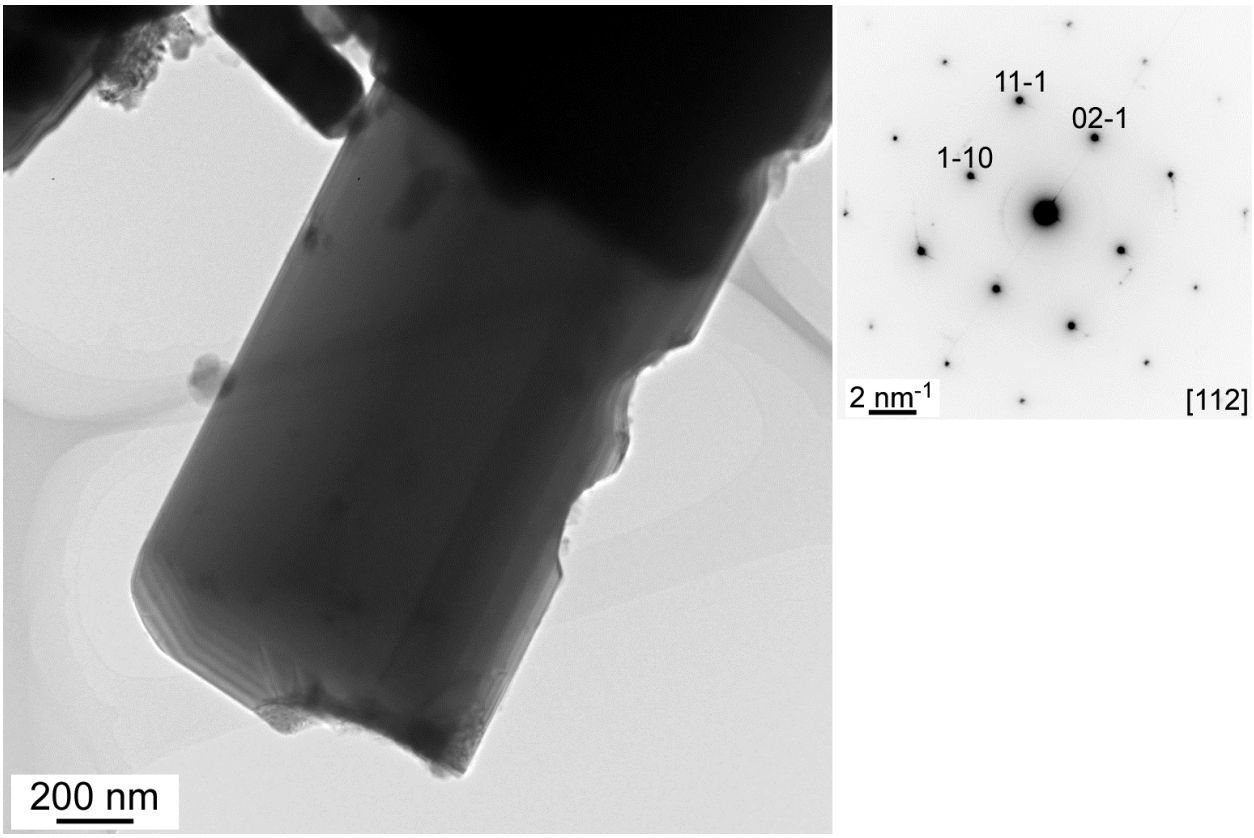

Figure 3.5 TEM direct image (left) and electron diffraction (right) of Cr2AlB2 after etching with KOH.

Discussion

The XRD patterns in **Figure 3.1** make a strong case for interlayer separation. On the left side is mostly phase pure $AlFe_2B_2$, with a couple minor impurity peaks left over after dissolution in HCl. On the right side is the same sample after 24 hours in 25% NaOH. The top shows

peak shifts, broadening, and reduced intensity compared to the left side, all of which are indicative of nanoscale grains. Further, the most dramatic peak shifts are the (0 k 0) peaks, which correspond to the spacing perpendicular to the MB layers. By adjusting the parameters of the structure file to increase the length of the b direction and remove the aluminum atoms, a strikingly similar pattern was simulated. Patterns for all three phases as synthesized, after washing with HCl, and with hydroxide etching are shown in **Figures S3.5-S3.8**.

Etching is confirmed by SEM and EDX analysis of flakes gathered after Na/KOH treatment. In **Figure 3.2**, a flake morphology is clear for both iron and manganese samples. The iron structure looks like a partially etched scaffold, where etching has occurred but not delamination. The partial and periodic etching resembles the etching seen for MoAlB. [37] **Figure 3.3** shows just a couple of layers for a chromium sample drop cast onto a silicon substrate. Interestingly, both a needle-like and a hexagonal morphology are present. This trend in increasing delamination moving from iron to chromium is mirrored in the data gathered through DFT calculations done to determine the Bader partial charge on each atomic site, tabulated in **Table 3.1**. Calculations were performed on each of the structures, as well as theoretical models made by removing one, then both, of the aluminum sites. In all cases,

aluminum maintained a partial positive charge from 1.5-1.7, indicating that the aluminum atoms are donating into the MB layers. Although a mechanism has not been established yet, both standard reduction potentials and mechanisms published for MXenes[60,61] would suggest that upon etching the aluminum atom is fully oxidized to Al^{3+}, yielding $AlCl_3$ or $Al(OH)_3$, or $Al(OH)_4^-$ in basic solution. This is supported by observed gas evolution during etching. The difficulty in isolating pristine sheets up to this point stems from a residual negative surface charge, which is either innate to the MB layer itself or imparted by surface groups such as OH- and Cl-. This charge is compensated by Na^+ ions or by surface Al^{3+} ions, which subsequently oxidize in air. The former has been seen through SEM-EDX, and the latter through TEM-EDX. Understanding the surface charge will make it easier to rationalize the zeta potential between the MB surface and the solution, which in turn will allow for optimized solution processing conditions.

AFM was used to confirm the two-dimensional nature of the flakes, representative micrographs and height profiles shown in **Figure 3.4**. For each of the phases flakes were found that averaged 1 μm in diameter and varied from 2-6 nm in thickness, 2.5 nm being typical. It was found in all cases that bulkier particulate was present in the dispersion along with the flakes, which centrifugation helped to

eliminate. The Fe_2AlB_2 samples are intriguing, as they all demonstrate a somewhat regular circular shape, within which are larger particles 20-40 nm thick. These embedded particles are always arranged in a circle or hexagonal arrangement, while the middle of the flake either has nothing embedded or has a flat step, with the embedded particles on the perimeter of this step.

Because of the amphoteric nature of aluminum and its oxides and hydroxides, both acidic and basic conditions are viable for removing aluminum from the structure. However, care needs to be taken to not go from an acidic environment to basic or vice-versa, as aluminum ions are not soluble in neutral pH and will either precipitate as alumina from acidic pH or form a hydroxide gel from basic pH. Other etchants have been tried including: acetic acid, HCl with KCl salt, citric acid, and triethylamine (TEA) with dimethyl sulfoxide (DMSO) and a small amount of water. The results are outlined in Table 3.2 below:

Table 3.2 Summary of etchants tested and their relative strengths and weaknesses

Etchant	XRD phases post washing	Pros	Cons
25% NaOH	M_2AlB_2 phase w/ shifted peaks and intensities	Showed most promise in XRD measurements	Na layer was evident from SEM, obscured sheets
25% KOH	M_2AlB_2 phase w/ shifted peaks and intensities	No K layer, data still suggests majority etched	Al_2O_3 in TEM
6 M HCl	M_2AlB_2 phase w/ slightly shifted peaks	Remove impurities simultaneously, H^+ may help neutralize surface	Etching less substantial
2.5 M HCl + $FeCl_3$	$Al_{13}Fe_4$, possible Fe_2B signal	Fe(III) could reduce instead of H^+, less bubbles to damage the sheets	Boride phase indistinguishable, water repellant foam formed at bottom of flask
5.8 M Acetic acid	M_2AlB_2 phase w/ moderately shifted peaks	More effective than HCl, behaves as chelating agent	
6 M HCl + KCl	Al_2O_3		Boride phase indistinguishable with XRD

Future Work

The largest gap in the understanding of this material at this point is in regard to the surface chemistry. The chemical environment at the surface and the adsorbed functional groups will have a large impact on

the properties of these materials, an area which has not been thoroughly studied as of yet. X-ray photoelectron spectroscopy and Raman/IR measurements would be crucial in this regard. The choice of etchant will control how the surface is terminated, which is intimately linked with the material properties. Dynamic light scattering would also be useful both for determining particle size as well as estimating the zeta potential of the MB surface. This information will be crucial to rationalize surface reaction mechanisms and intercalation behavior.

Based on the results thus far, it is possible to obtain highly uniform platelets with a small diameter which may prove useful for catalysis. A couple preliminary measurements have been run for both hydrogen evolution and oxygen reduction reactions, which showed modest activity. These samples would need to be further purified before any conclusions can be drawn about their potential. The potential of these materials as battery electrodes, however, could be examined immediately as it isn't necessary to delaminate the structure for this application. It has been demonstrated that the majority of the aluminum can be removed from the structure, which can be controlled via etching time as well as by choice of etchant. There are options for tuning the cation intercalation chemistry, and this work serves as a starting point for someone wishing to do so.

Once this method has successfully been applied to the AlM_2B_2 structure new bulk targets can be investigated, such as the MoAlB structure[37], the $(CrB_2)_nCrAl$ structures[20], or the theoretical $Li_{2(1-x)}Al_xB_2$ structure.[62]

References

1 M.T. Yeung, R. Mohammadi, R.B. Kaner, *Annu. Rev. Mater. Res.*, 2016, **46**, 465–485.

2 J. Nagamatsu, N. Nakagawa, T. Muranaka, Y. Zenitani, J. Akimitsu, *Nature*, 2001, **410**, 63–64.

3 H. Park, A. Encinas, J.P. Scheifers, Y. Zhang, B.P.T. Fokwa, *Angew. Chemie - Int. Ed.*, 2017, **56**, 5575–5578.

4 B.P.T. Fokwa, *Eur. J. Inorg. Chem.*, 2010, **2010**, 3075–3092.

5 J.P. Scheifers, Y. Zhang, B.P.T. Fokwa, *Acc. Chem. Res.*, 2017, **50**, 2317–2325.

6 B. Albert, H. Hillebrecht, *Angew. Chemie - Int. Ed.*, 2009, **48**, 8640–8668.

7 T. Mori, *J. Phys. Conf. Ser.*, 2009, **176**, 012036.

8 G. Akopov, M.T. Yeung, R.B. Kaner, *Adv. Mater.*, 2017, 1604506.

9 P. Villars, L.D. Calvert, 『Person's Handbook of Crystallographic Data for Intermetallic Phases』, CD-ROM ed., ASM International, Materials Park OH, 1991.

10 Y.P. Kuz'ma, Yu.B.; Yarmolyuk, *Zhurnal Strukt. Khimii*, 1971, **12**, 458.

11 M. Ade, D. Kotzott, H. Hillebrecht, *J. Solid State Chem.*, 2010, **183**, 1790–1797.

12 T. Lundstrom, *Pure Appl. Chem.*, 1985, **57**, 1383–1390.

13 T. Mori, H. Borrmann, S. Okada, K. Kudou, A. Leithe-Jasper, U. Burkhardt, Y. Grin, *Phys. Rev. B*, 2007, **76**, 064404.

14 J. Bauer, J.-F. Halet, J.-Y. Saillard, *Coord. Chem. Rev.*, 1998, **178–180**, 723–753.

15 T. Mori, *Handb. Phys. Chem. Rare Earths*, 2007, **38**, 105–173.

16 P.I. Chepiga, M.V.; Kuzma, Yu.B.; Kripyakevich, *Dopovidi Akad. Nauk Ukr. RSR, Seriya A Fiz. Ta Mat. Nauk.*, 1972, 856–858.

17 B.P.T. Fokwa, M. Hermus, *Angew. Chemie Int. Ed.*, 2012, **124**, 1734–1737.

18 C. Goerens, B.P.T. Fokwa, *J. Solid State Chem.*, 2012, **192**, 113–119.

19 Q. Zheng, R. Gumeniuk, H. Rosner, W. Schnelle, Y. Prots, U. Burkhardt, Y. Grin, A. Leithe-Jasper, *J. Phys. Condens. Matter*, 2015, **27**, 415701.

20 M. Ade, H. Hillebrecht, *Inorg. Chem.*, 2015, **54**, 6122–6135.

21 J. Lu, S. Kota, M.W. Barsoum, L. Hultman, *Mater. Res. Lett.*, 2017, **5**, 235–241.

22 Y. Zhou, H. Xiang, F.Z. Dai, Z. Feng, *Mater. Res. Lett.*, 2017, **5**, 440–448.

23 M. Naguib, M. Kurtoglu, V. Presser, J. Lu, J. Niu, M. Heon, L. Hultman, Y. Gogotsi, M.W. Barsoum, *Adv. Mater.*, 2011, **23**, 4248–4253.

24 V.M. Hong Ng, H. Huang, K. Zhou, P.S. Lee, W. Que, J.Z. Xu, L.B. Kong, *J. Mater. Chem. A*, 2017, **5**, 3039–3068.

25 K. Maleski, V.N. Mochalin, Y. Gogotsi, *Chem. Mater.*, 2017, **29**, 1632–1640.

26 B. Anasori, M.R. Lukatskaya, Y. Gogotsi, *Nat. Rev. Mater.*, 2017, **2**, 16098.

27 M. Khazaei, A. Ranjbar, M. Arai, T. Sasaki, S. Yunoki, *J. Mater. Chem. C*, 2017, **5**, 2488–2503.

28 T. Ouisse, M.W. Barsoum, *Mater. Res. Lett.*, 2017, **5**, 365–378.

29 M.R. Lukatskaya, S. Kota, Z. Lin, M.-Q. Zhao, N. Shpigel, M.D. Levi, J. Halim, P.-L. Taberna, M.W. Barsoum, P. Simon, Y. Gogotsi, *Nat. Energy*, 2017, **6**, 17105.

30 Z.W. Seh, K.D. Fredrickson, B. Anasori, J. Kibsgaard, A.L. Strickler, M.R. Lukatskaya, Y. Gogotsi, T.F. Jaramillo, A. Vojvodic, *ACS Energy Lett.*, 2016, **1**, 589–594.

31 X. Zhang, Z. Zhang, J. Li, X. Zhao, D. Wu, Z. Zhou, *J. Mater. Chem. A*, 2017, **5**, 12899–12903.

32 R. Li, L. Zhang, L. Shi, P. Wang, *ACS Nano*, 2017, **11**, 3752–3759.

33 B.P.T. Fokwa, *Encycl. Inorg. Bioinorg. Chem.*, 2014, 1–14.

34 R. Barua, B.T. Lejeune, L. Ke, G. Hadjipanayis, E.M. Levin, R.W. McCallum, M.J. Kramer, L.H. Lewis, *J. Alloys Compd.*, 2018, **745**, 505–512.

35 A.L. James, K. Jasuja, *RSC Adv.*, 2017, **7**, 1905–1914.

36 Z. Guo, J. Zhou, Z. Sun, *J. Mater. Chem. A*, 2017,.

37 L.T. Alameda, C.F. Holder, J.L. Fenton, R.E. Schaak, *Chem. Mater.*, 2017, **29**, 8953–8957.

38 H. Zhang, H. Xiang, F. zhi Dai, Z. Zhang, Y. Zhou, *J. Mater. Sci. Technol.*, 2018,.

39 S. Rundqvist, S. Pramatus, B. Lamm, A. Haug, H. Theorell, R. Blinc, S. Paušak, L. Ehrenberg, J. Dumanović, *Acta Chem. Scand.*, 1967, **21**, 191–194.

40 Z. Malik, A. Grytsiv, P. Rogl, G. Giester, J. Bursik, *J. Solid State Chem.*, 2013, **198**, 150–161.

41 S. Hirt, F. Hilfinger, H. Hillebrecht, *Zeitschrift Für Krist. - Cryst. Mater.*, 2018, **6**, 1–14.

42 R. St. Touzani, M. Mbarki, X. Chen, B.P.T. Fokwa, *Eur. J. Inorg.*

Chem., 2016, **2016**, 4104–4110.

43 A.R. Oganov, A.O. Lyakhov, M. Valle, *Acc. Chem. Res.*, 2011, **44**, 227–237.

44 A.O. Lyakhov, A.R. Oganov, H.T. Stokes, Q. Zhu, *Comput. Phys. Commun.*, 2013, **184**, 1172–1182.

45 A.R. Oganov, C.W. Glass, *J. Chem. Phys.*, 2006, **124**, 244704.

46 M. Mbarki, R. St. Touzani, B.P.T. Fokwa, *Eur. J. Inorg. Chem.*, 2014, **2014**, 1381–1388.

47 O. Schob, E. Parthé, *Acta Crystallogr.*, 1965, **19**, 214–224.

48 R. Dronskowski, P.E. Bloechl, *J. Phys. Chem.*, 1993, **97**, 8617–8624.

49 M. Mbarki, R.S. Touzani, C.W.G. Rehorn, F.C. Gladisch, B.P.T. Fokwa, *J. Solid State Chem.*, 2016, **242**, 28–33.

50 J. Rodriguez-Carvajal, FULLPROF 2000: A Rietveld Refinement and Pattern Matching Analysis Program, 2008.

51 G.M. Sheldrick, *Acta Crystallogr. Sect. A Found. Crystallogr.*, 2007, **64**, 112–122.

52 G.M. Sheldrick, *Acta Crystallogr. Sect. C Struct. Chem.*, 2015, **71**, 3–8.

53 G.M. Sheldrick, 1996,.

54 G. Kresse, D. Joubert, *Phys. Rev. B*, 1999, **59**, 1758–1775.

55 P.E. Blöchl, *Phys. Rev. B*, 1994, **50**, 17953–17979.

56 J.P. Perdew, K. Burke, M. Ernzerhof, *Phys. Rev. Lett.*, 1996, **77**, 3865–3868.

57 R.W. Tank, O. Jepsen, *Cell*, 1998, 1–27.

58 W. Kohn, L.J. Sham, *Phys. Rev.*, 1965, **140**, 1133–1138.

59 P.-O. Lowdin, *J. Chem. Phys.*, 1951, **19**, 1396–1171.

60 W. Sun, S.A. Shah, Y. Chen, Z. Tan, H. Gao, T. Habib, M. Radovic, M.J. Green, n.d.,.

61 J. Wen, X. Zhang, H. Gao, *Phys. B Condens. Matter*, 2018, **537**, 155–161.

62 A.N. Kolmogorov, M. Calandra, S. Curtarolo, *Phys. Rev. B - Condens. Matter Mater. Phys.*, 2008, **78**, .

Chapter 4: Conclusions and Perspective

A new ternary boride structure has been discovered, with a unique combination of structural motifs common to other borides with higher and lower M:B ratios. Both infinite boron chains (FeB fragment) and isolated boron atoms within trigonal prisms (Re_3B fragment) are present. Single crystal XRD confirms partial substitution of osmium onto the niobium sites, indicating that the stoichiometric structure is electron deficient. DFT and COHP analysis were performed to show unfilled bonding states in the theoretical stoichiometric NbOsB phase, which was combined with structural analysis to explain the partial substitution of osmium onto the niobium sites. It was observed that a small number of Nb-Nb and Nb-B bonds were highly stabilized at the cost of a large number of slightly unfavorable Os-Nb and Os-B interactions. This localized stabilization compensates for the highly compressed FeB fragment. It is predicted that a group 6 metal would be more appropriate for the niobium site, and that a larger metal on the osmium site may help relieve internal strain between the osmium and niobium substructures. Future works may be able to use this to form a stabilized version of the crystal structure. If the phase pure compound could be produced from a stoichiometric melt, this would make it possible to study potential properties of this structure. Both

TaRuB and NbOsB are low temperature superconductors. [19] The relatively high DOS at E_F suggests an instability of some sort, which could resolve itself through structural distortions or electron ordering such as superconductivity.

Progress has been made in exfoliating M_2AlB_2 structures into 2D layers. The largest gap in the understanding of this material at this point is in regard to the surface chemistry. The chemical environment at the surface and the adsorbed functional groups will have a large impact on the properties of these materials, an area which has not been thoroughly studied as of yet. X-ray photoelectron spectroscopy and Raman/IR measurements would be crucial in this regard. The choice of etchant will control how the surface is terminated, which is intimately linked with the material properties. This information will be crucial to rationalize surface reaction mechanisms and intercalation behavior.

Based on the results thus far, it is possible to obtain highly uniform platelets with a small diameter which may prove useful for catalysis. A couple preliminary measurements have been run for both hydrogen evolution and oxygen reduction reactions, which showed modest activity. These samples would need to be further purified before any conclusions can be drawn about their potential. The potential of these

materials as battery electrodes, however, could be examined immediately as it isn't necessary to delaminate the structure for this application. It has been demonstrated that the majority of the aluminum can be removed from the structure, which can be controlled via etching time as well as by choice of etchant. There are options for tuning the cation intercalation chemistry, and this work serves as a starting point for someone wishing to do so.

Table S2.1 Parameters of the Rietveld powder refinement.

Phase	$Nb_{(1-x)}Os_{(1+x)}B$	Os
space group, *Z*	*Pnma (no. 61); 6*	$P\frac{63}{m}mc$ *(no. 194); 1*
a (Å)	11.2782(6)	2.7352(1)
b (Å)	3.003(2)	-
c (Å)	12.901(7)	4.3296(3)
V (Å^3)	436.9(4)	28.051(2)
2θ-range (°)	10-82.9	
refinement method	least squares	
profile function	pseudo-Voigt	
R_{Bragg}	6.89	7.89
Weight fraction	62.4(9) [a]	37.6(3) [a]

a) relative due to unidentified reflections in the powder XRD data

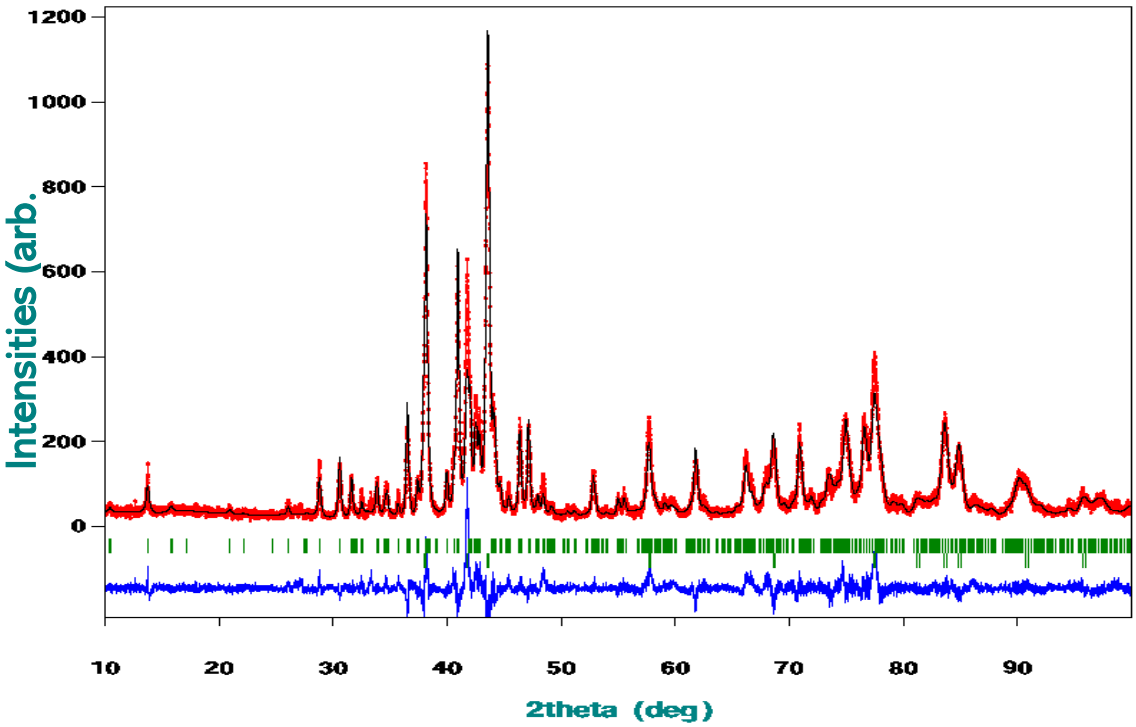

Figure S2.2 Rietveld refinement of the powder data for $Nb_{(1-x)}Os_{(1+x)}B$, showing measured (red) and fitted intensities (black). The green lines are the position of the Bragg reflections for the product and osmium metal. The difference intensity curve is in blue. A small peak at 33° could not be matched to any existing phases

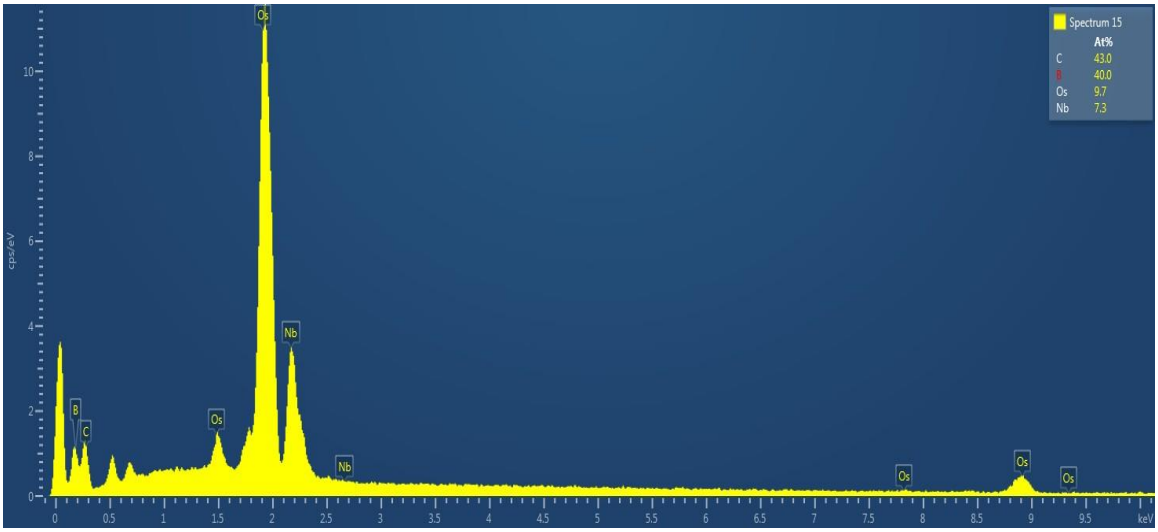

Figure S2.3 EDX spectra for a $Nb_{1-x}Os_{1+x}B$ single crystal, which supports an excess of osmium. Carbon peak is from carbon paste used to support the sample.

Table S2.4 *Atom positions, site occupation factors (s.o.f.) and displacement parameters. All atomic positions are at 4c Wyckoff sites*

Atom	x	y	z	*s.o.f.*	U_{11}	U_{22}	U_{33}	U_{13}	U_{eq}
Os1	0.6760 (1)	¼	0.5915 (1)	1	0.0103 (5)	0.0142 (5)	0.0047 (4)	-0.0004 (4)	0.0097 (2)
Os2	0.2999 (1)	¼	0.7128 (1)	1	0.0100 (5)	0.0091 (5)	0.0001 (4)	0.0001 (4)	0.0079 (2)
Os3	0.0440 (1)	¼	0.7282 (1)	1	0.0090 (5)	0.0095 (5)	0.0002 (4)	0.0002 (4)	0.0085 (2)
Nb1/ Os4	0.0346 (2)	¼	0.0945 (1)	0.81(1)/ 0.19(1)	0.013 (1)	0.0109 (9)	0.0061 (9)	0.0003 (6)	0.0101 (6)
Nb2/ Os5	0.1157 (2)	¼	0.3826 (2)	0.80(1)/ 0.20(1)	0.015 (1)	0.011 (1)	0.0086 (9)	0.0013 (7)	0.0116 (6)
Nb3/ Os6	0.3399 (2)	¼	0.0756 (2)	0.90(1)/ 0.10(1)	0.012 (1)	0.008 (1)	0.0065 (9)	-0.0032 (7)	0.0090 (6)
B1	0.325 (3)	¼	0.272 (2)	1	-	-	-	-	0.007 (5)
B2	0.006 (3)	¼	0.536 (3)	1	-	-	-	-	0.021 (7)
B3	0.321 (3)	¼	0.529 (3)	1	-	-	-	-	0.011 (6)

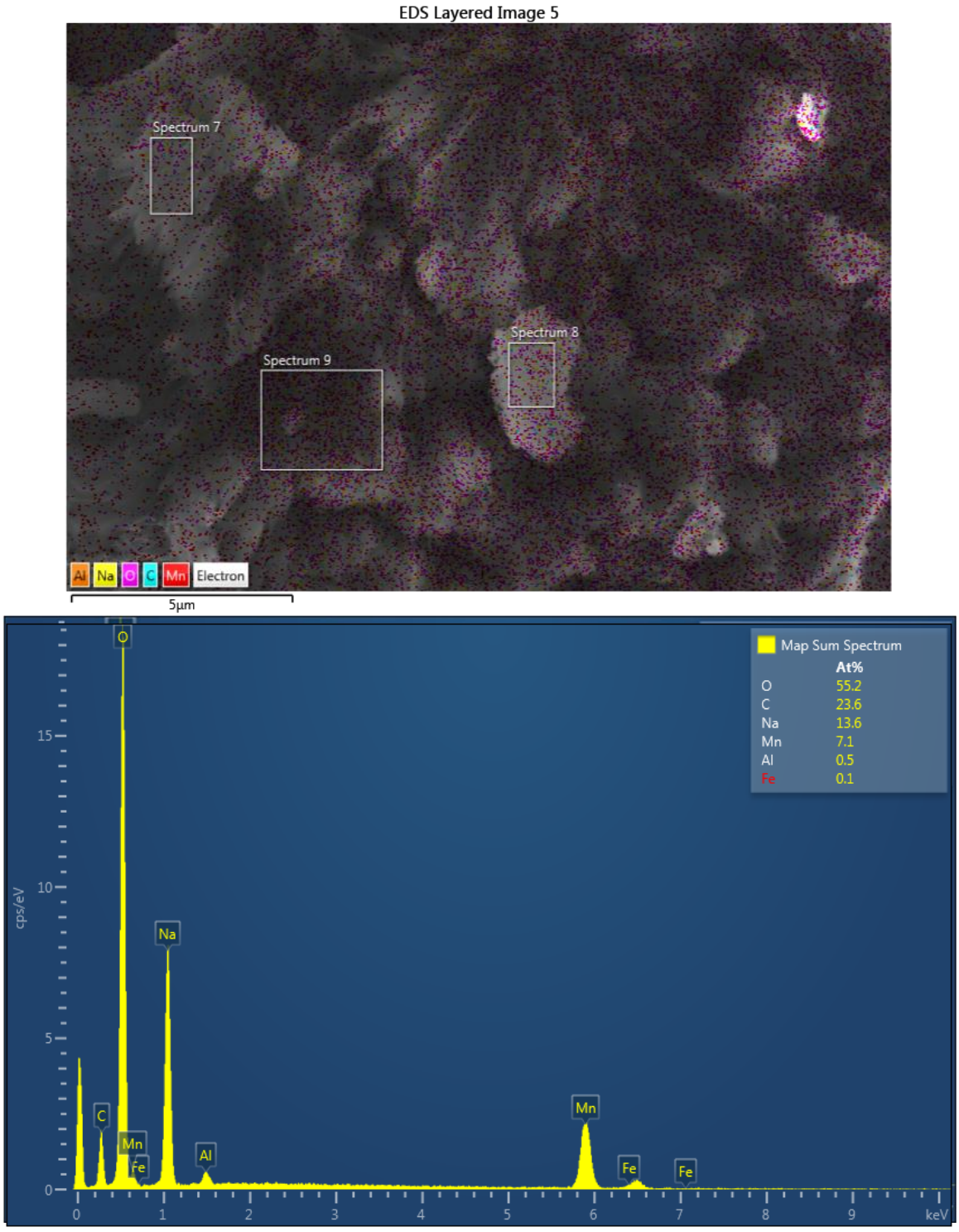

Figure S3.1 EDX mapping and spectra taken on sample shown in Figure 2.3 bottom. The ratio shown indicates ~86% aluminum removed. Notice the large sodium signal.

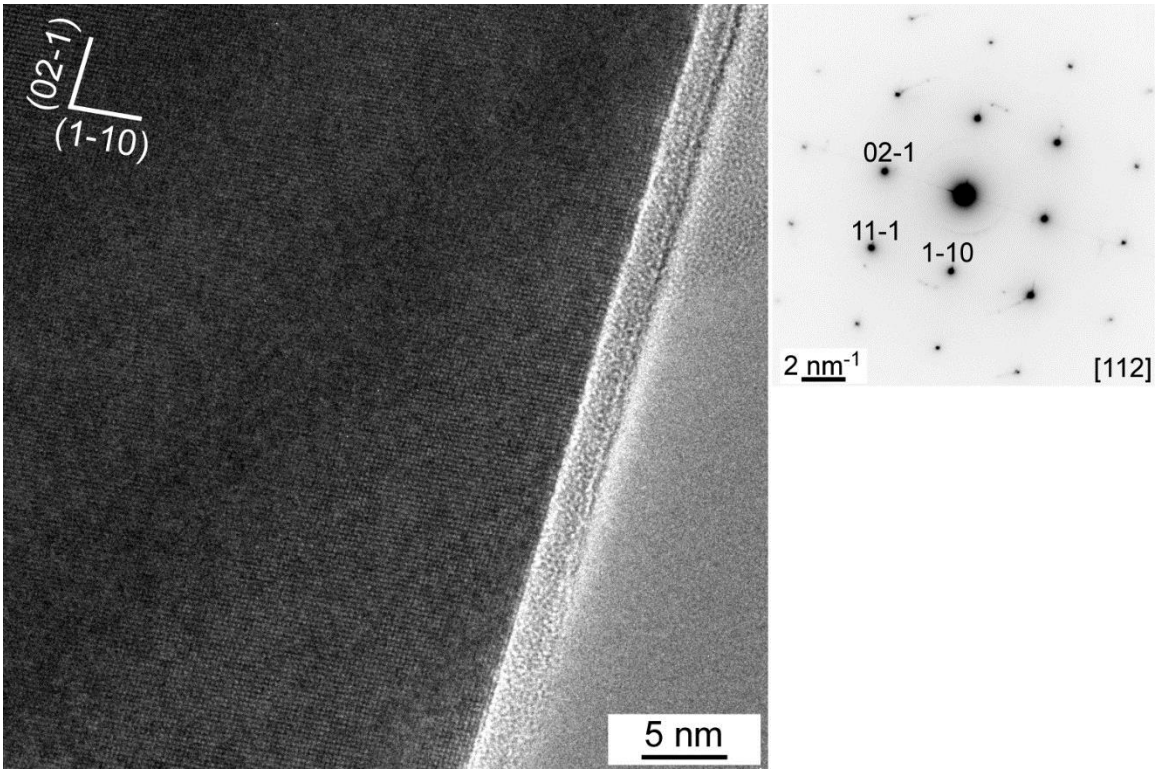

Figure S3.2 TEM image and diffraction pattern for an etched Cr_2AlB_2 sample. Planes of atoms are visible at this magnification, and there are no boundaries in the area imaged.

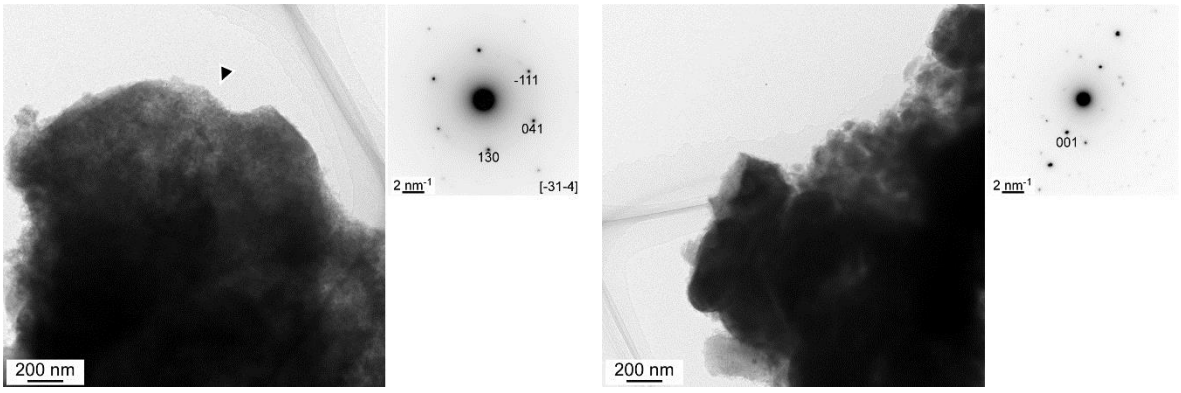

Figure S3.3 TEM image and diffraction pattern for an etched Mn_2AlB_2 sample (left) and Fe_2AlB_2 sample (right).

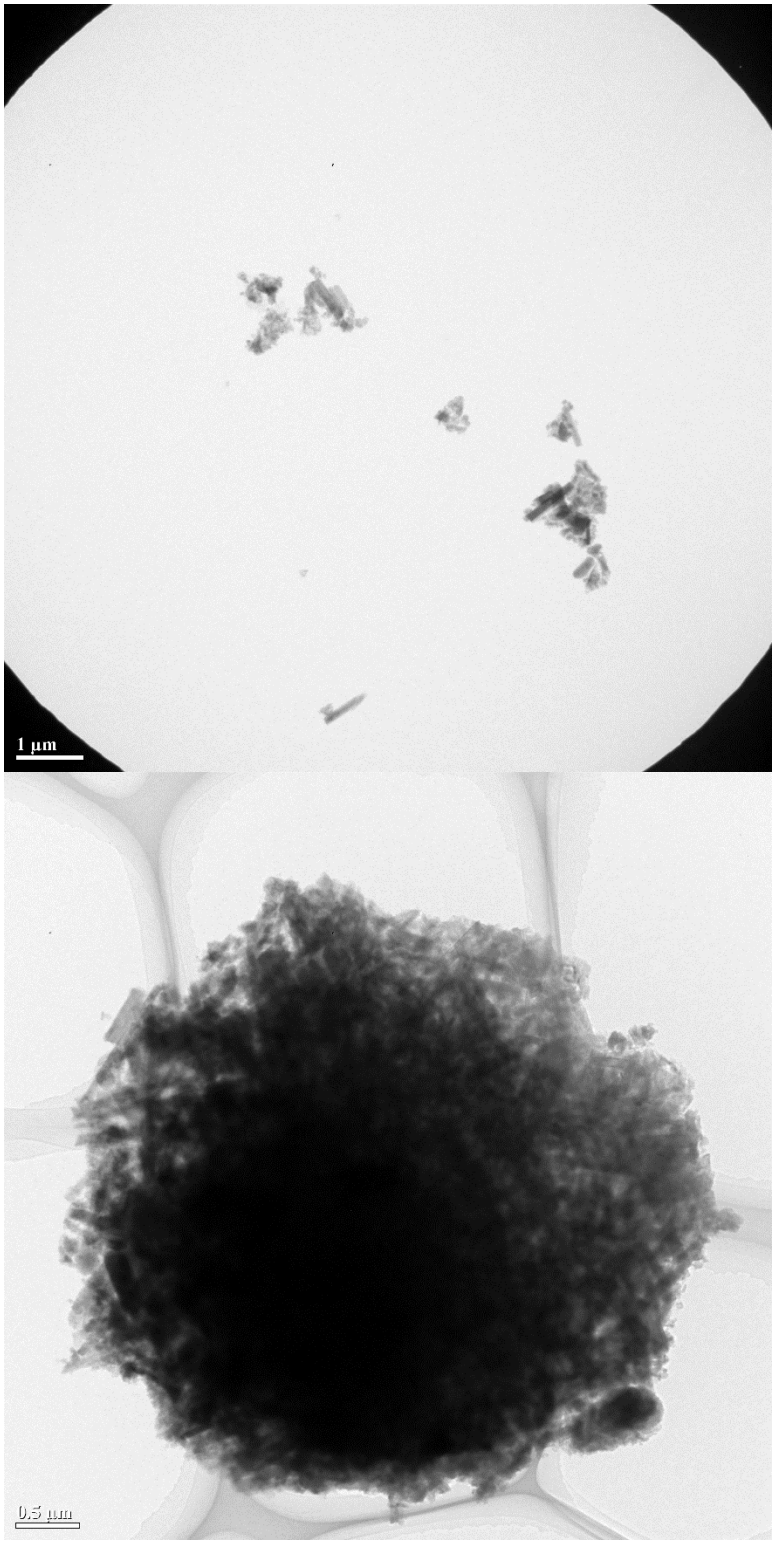

Figure S3.4 TEM direct images of Mn_2AlB_2 sample showing individual needle-like particles (top) and an agglomeration of these particles (bottom)

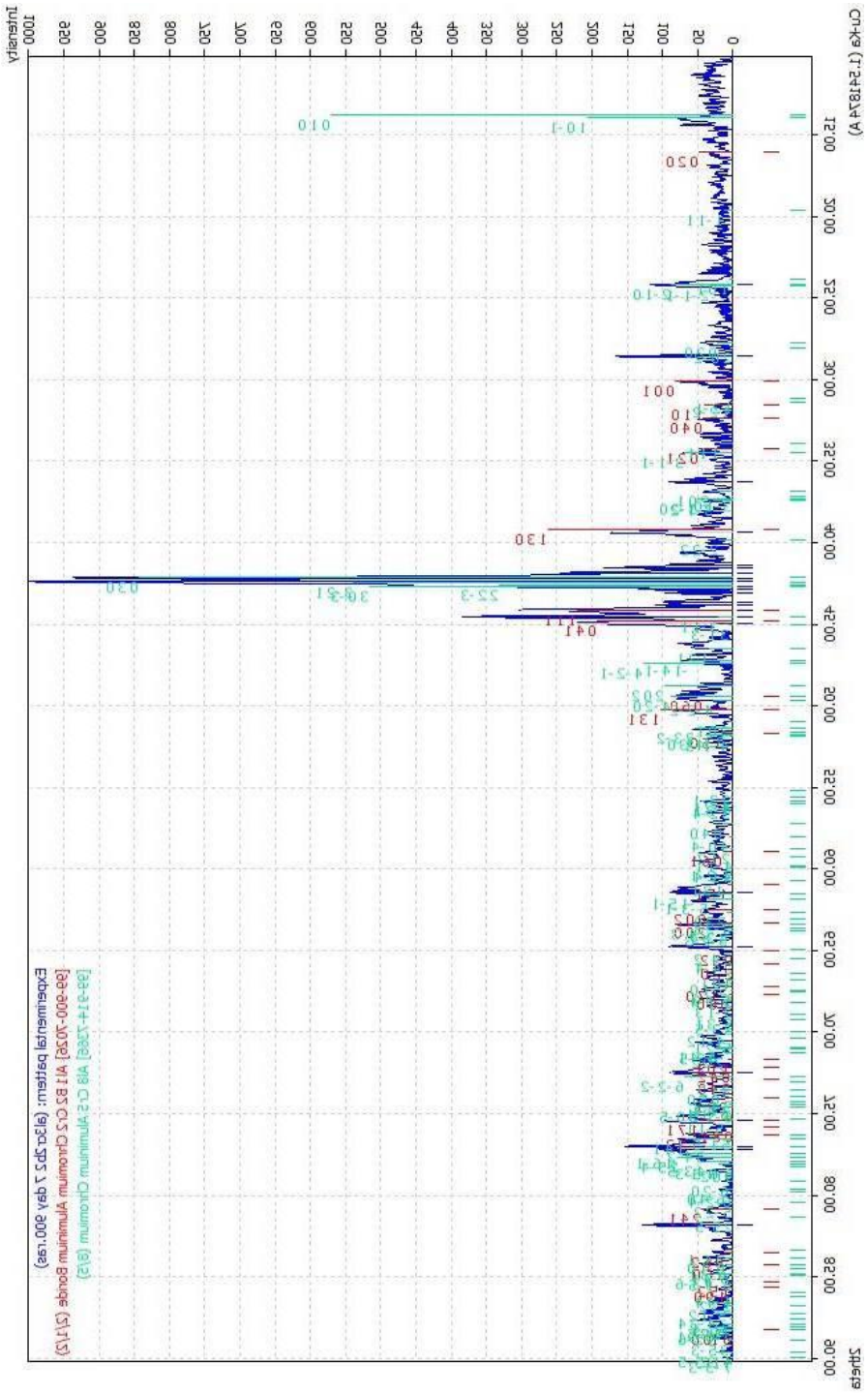

Figure S3.5 XRD diffractogram for Cr_2AlB_2 samples as synthesized. Peaks corresponding to Cr_2AlB_2 are shown in red while the major side product, Al_8Cr_5, is shown in green.

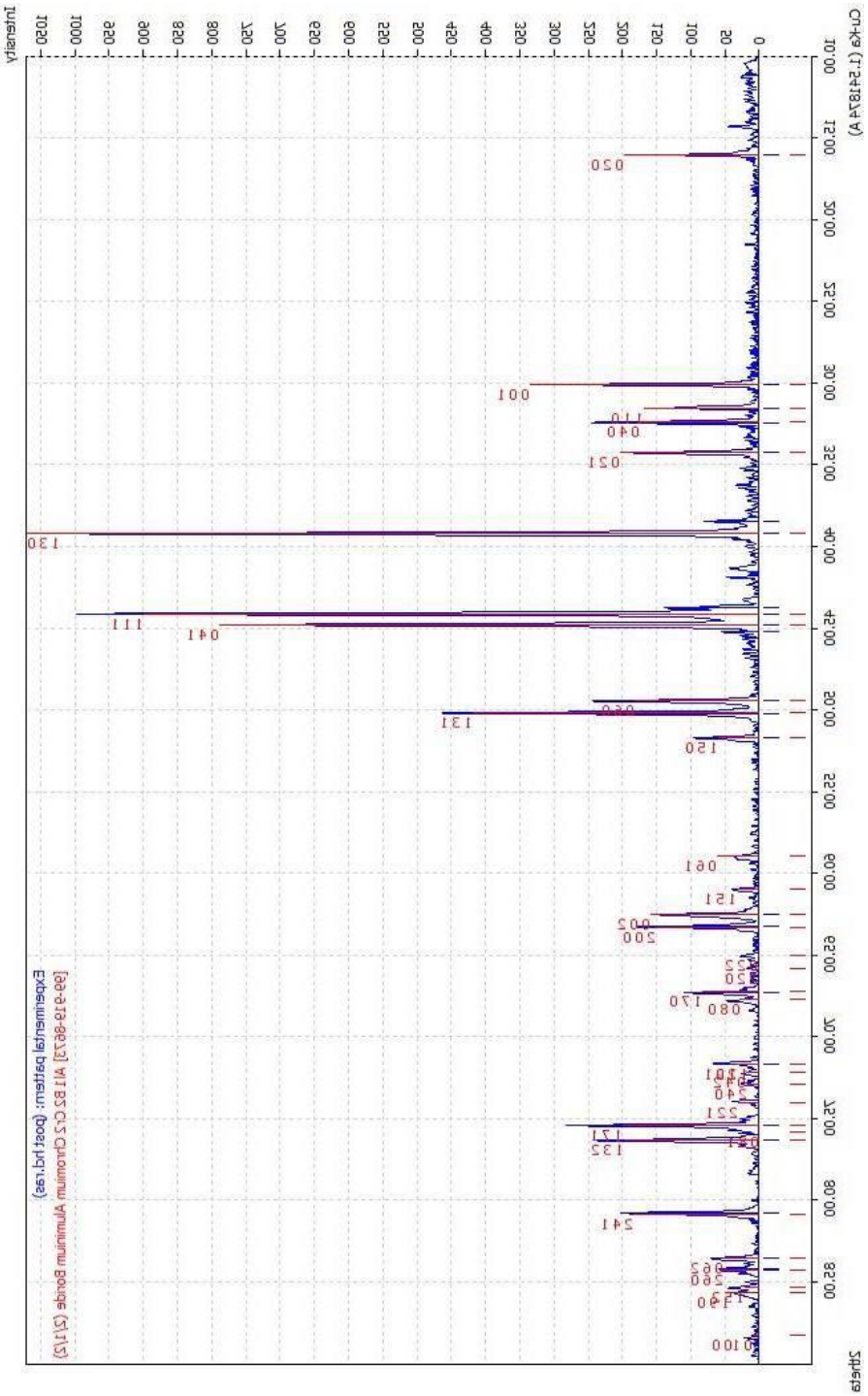

Figure S3.6 XRD diffractogram for Cr_2AlB_2 samples post HCl washing. Peaks corresponding to Cr_2AlB_2 are shown in red.

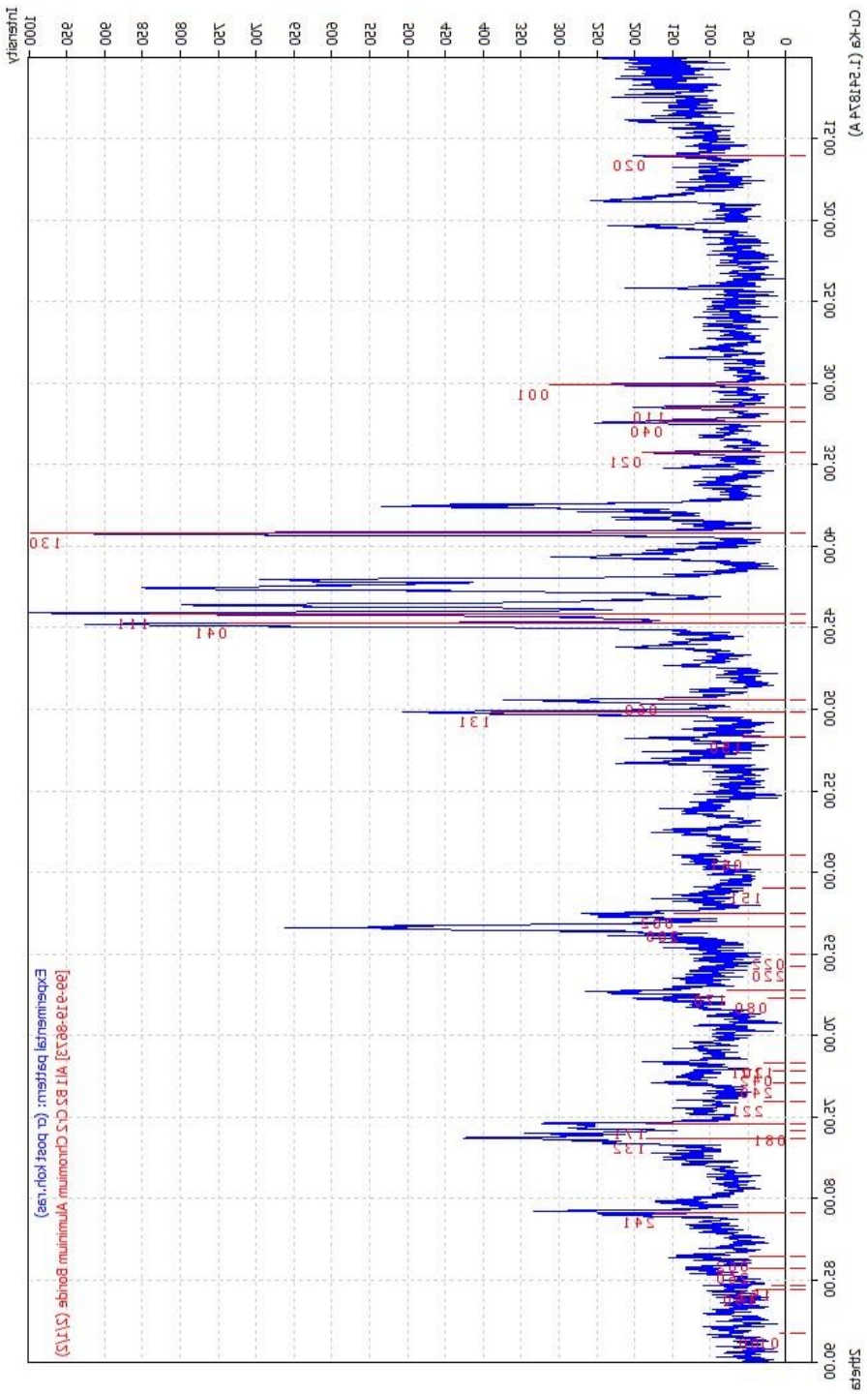

Figure S3.7 XRD diffractogram for Cr_2AlB_2 samples post etching with KOH. Post treatment the sample becomes more amorphous in nature, and additional peaks are seen.

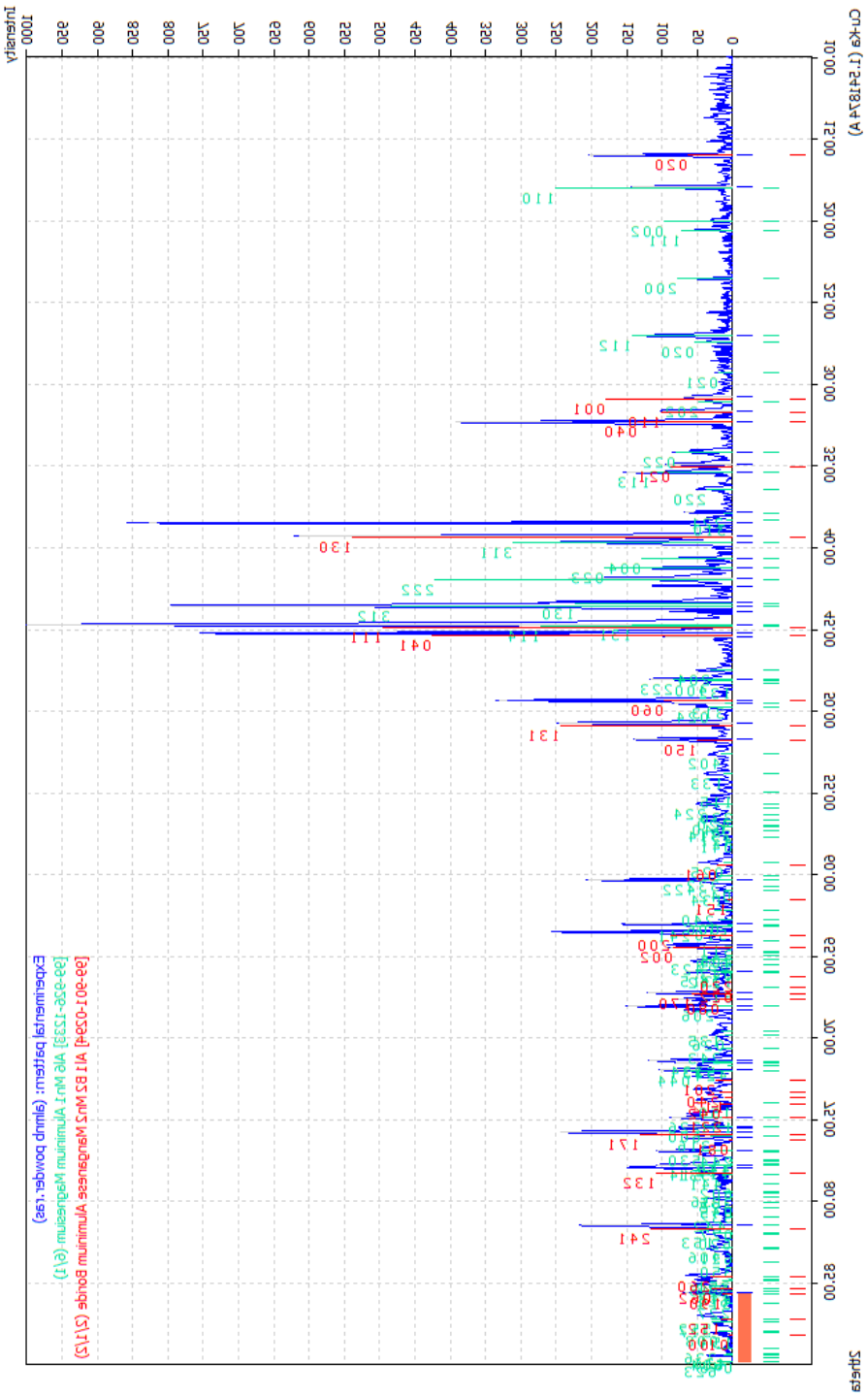

Figure S3.8 XRD diffractogram for Mn_2AlB_2 samples as synthesized. Peaks corresponding to Mn_2AlB_2 are shown in red while the major side product, Al_6Mn, is shown in green.

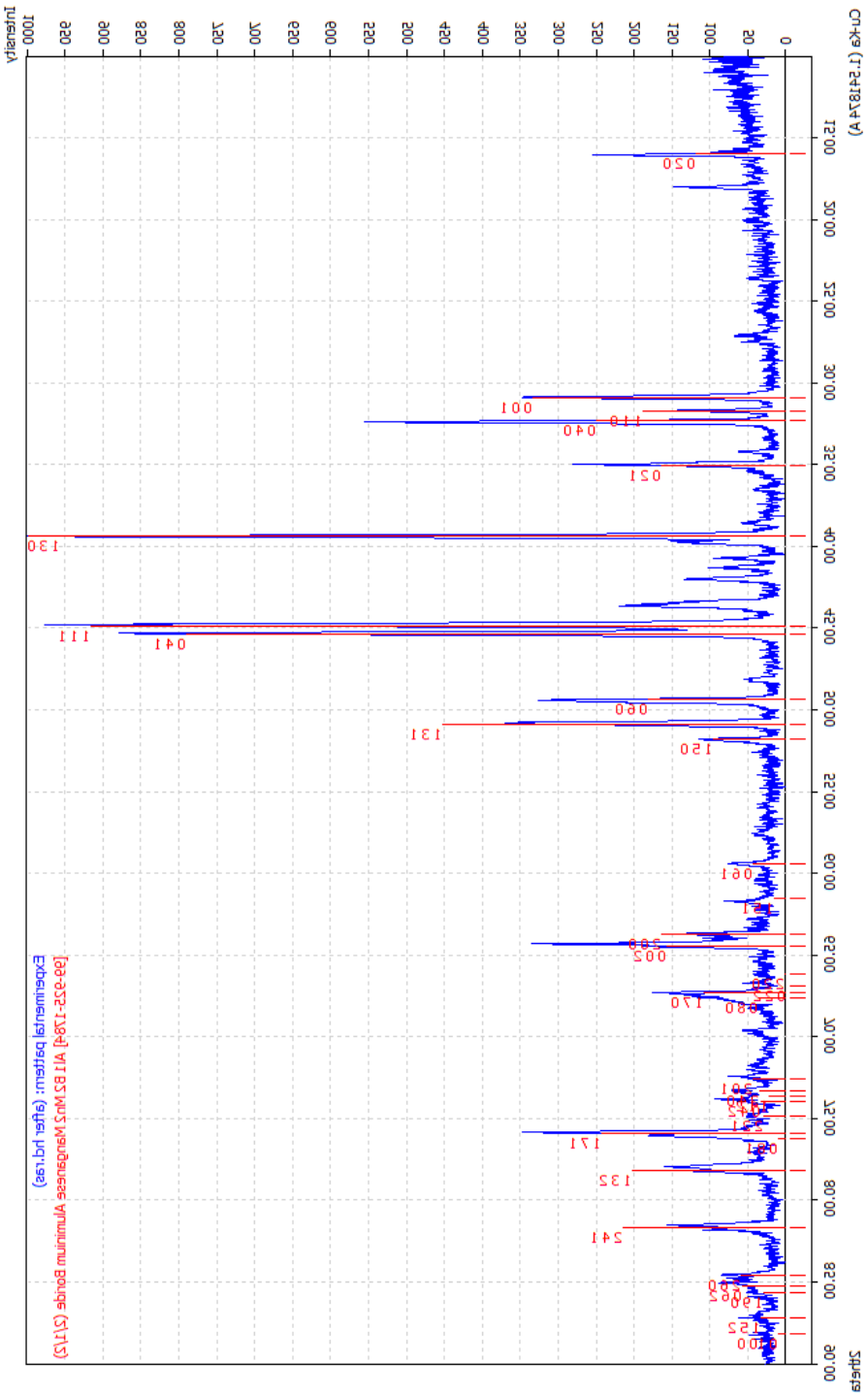

Figure S3.9 XRD diffractogram for Mn_2AlB_2 samples post HCl washing. Peaks corresponding to Mn_2AlB_2 are shown in red. There are still residual peaks from Al_xMn_y intermetallic phases.

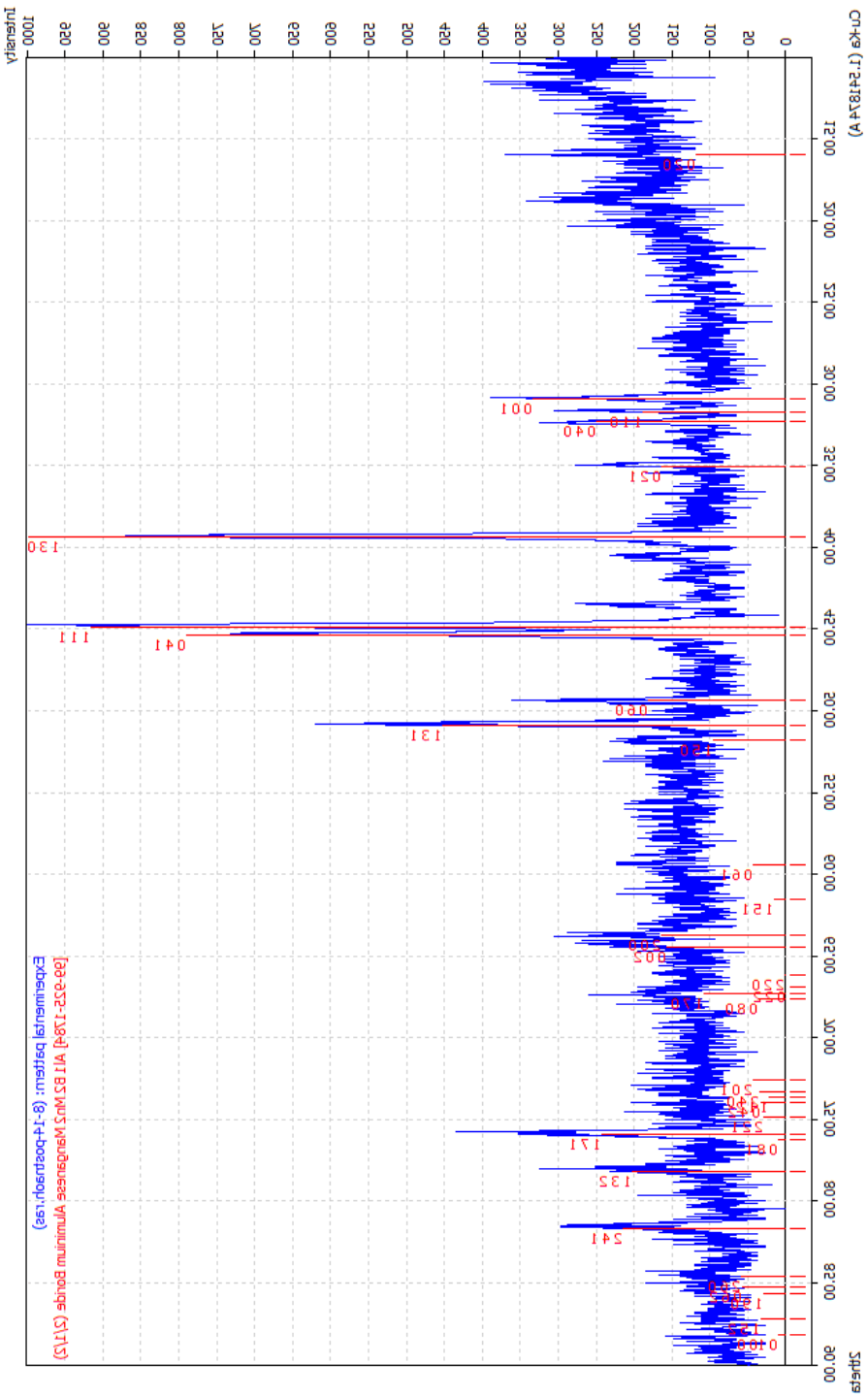

Figure S3.10 XRD diffractograms for Mn_2AlB_2 samples post etching with NaOH. Post NaOH the sample has become significantly amorphous, evident from the broad humps in the background.

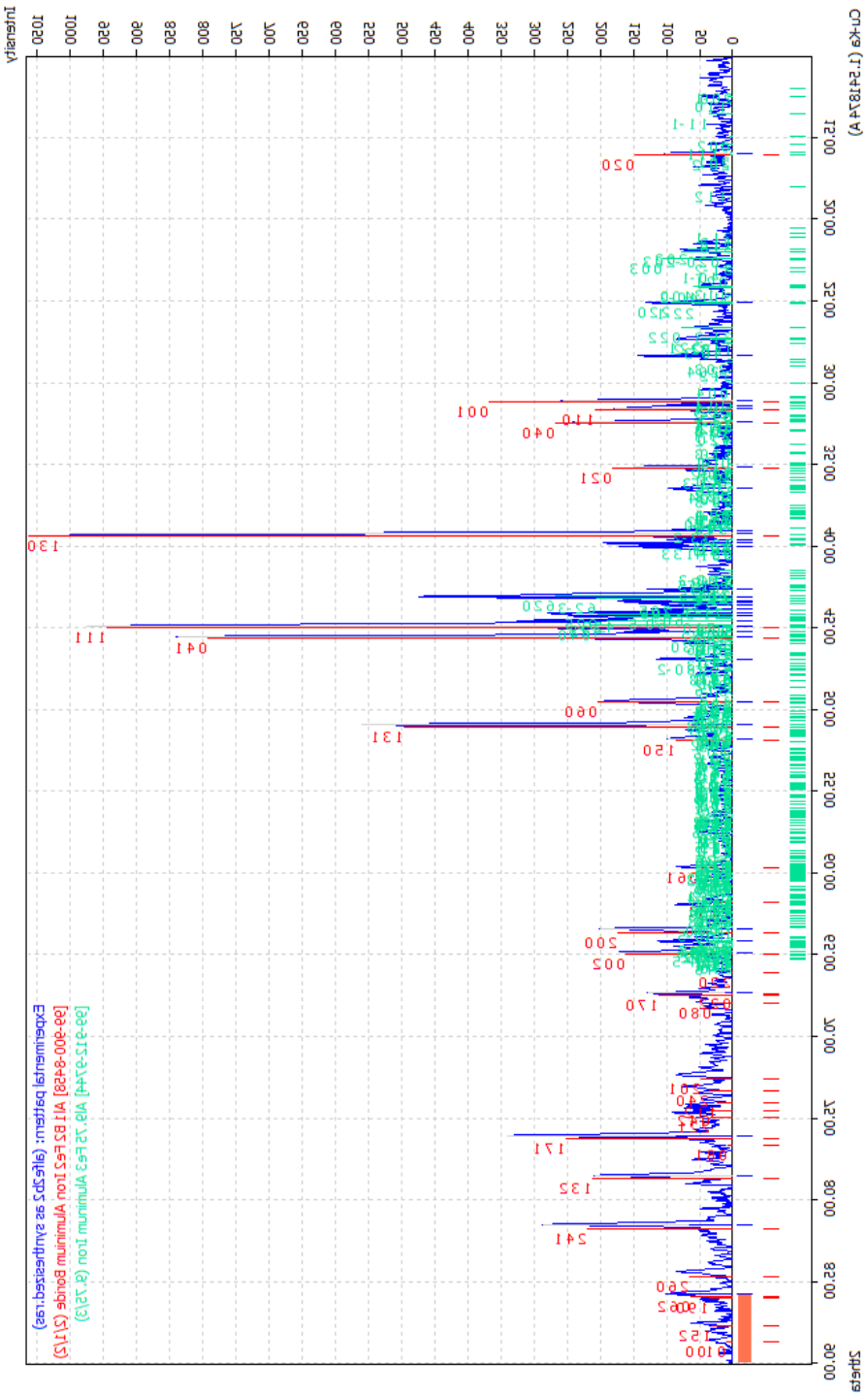

Figure S3.11 XRD diffractogram for Fe_2AlB_2 samples as synthesized. Peaks corresponding to Fe_2AlB_2 are shown in red while the major side product, $Al_{9.75}Fe_{13}$, is shown in green.

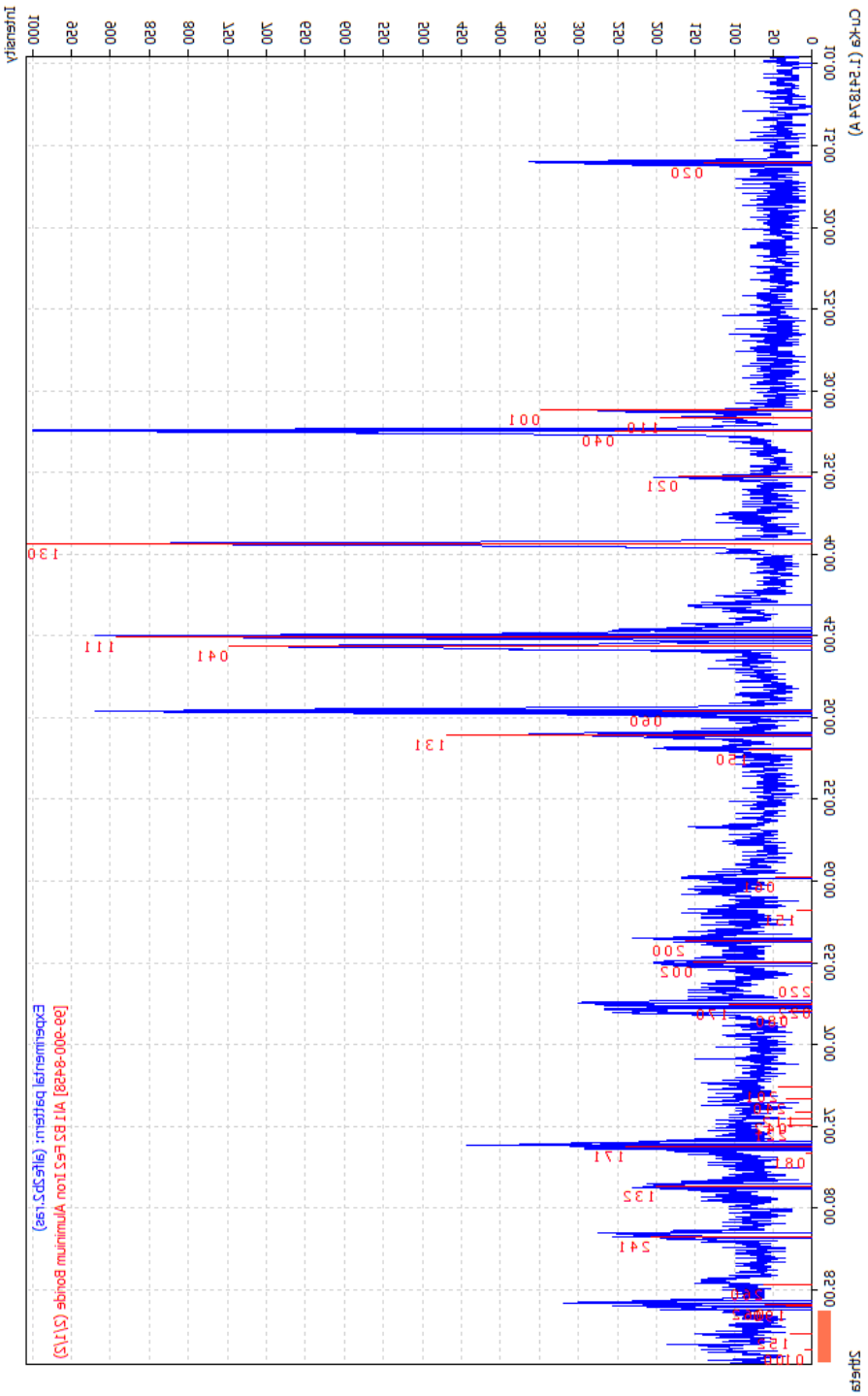

Figure S3.12 XRD diffractograms for Fe_2AlB_2 sample post HCl washing. Peaks corresponding to Mn_2AlB_2 are shown in red. The high background suggests reduced crystallinity, and the significantly higher (0 k 0) peaks suggest that partial etchin may have already occurred.

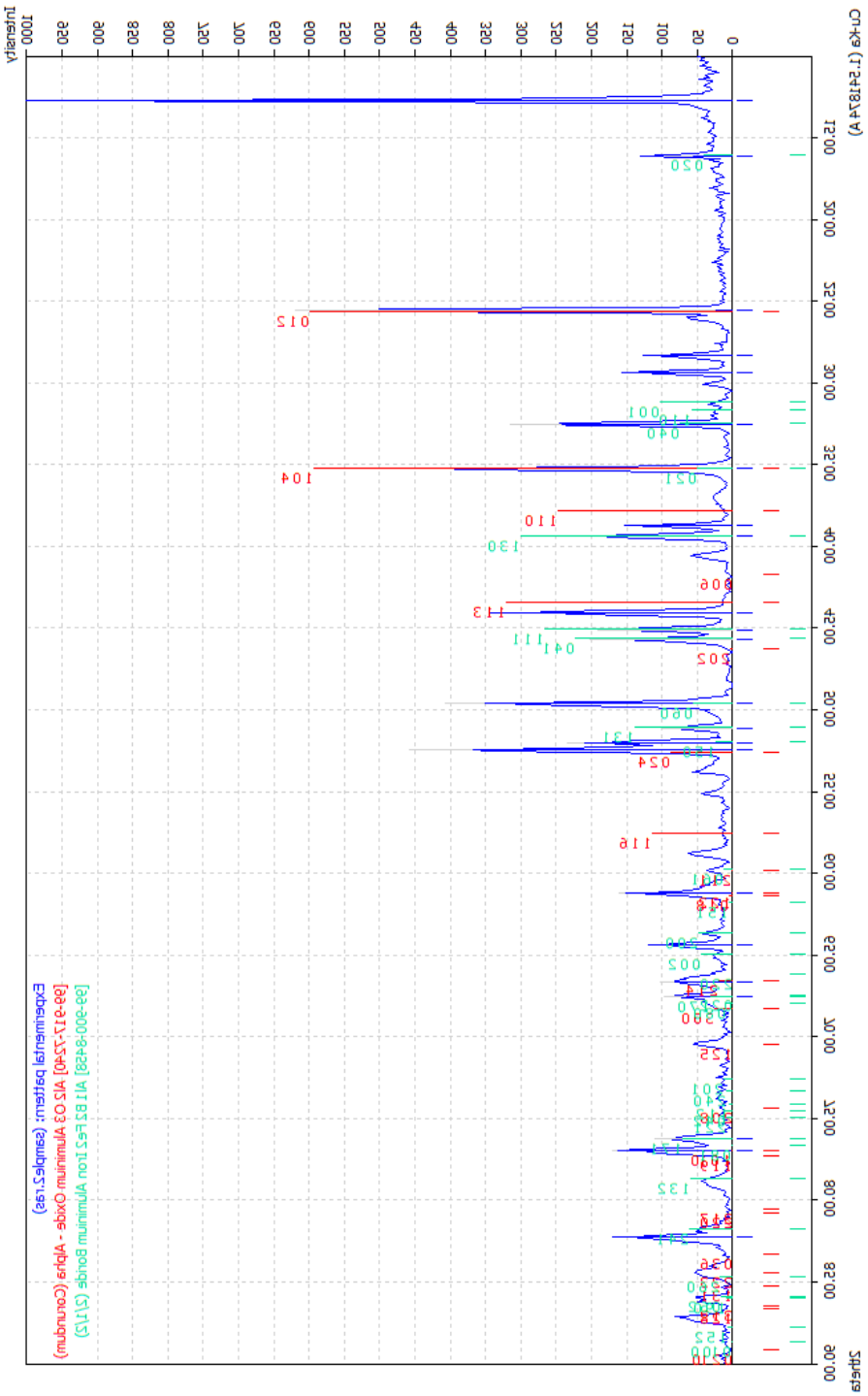

Figure S3.13 XRD diffractograms for Fe_2AlB_2 samples post etching with NaOH. Post NaOH the major phase has become Al2O3. It is possible that aluminum ions did not dissociate from the surface during washing, and subsequently oxidized upon drying.

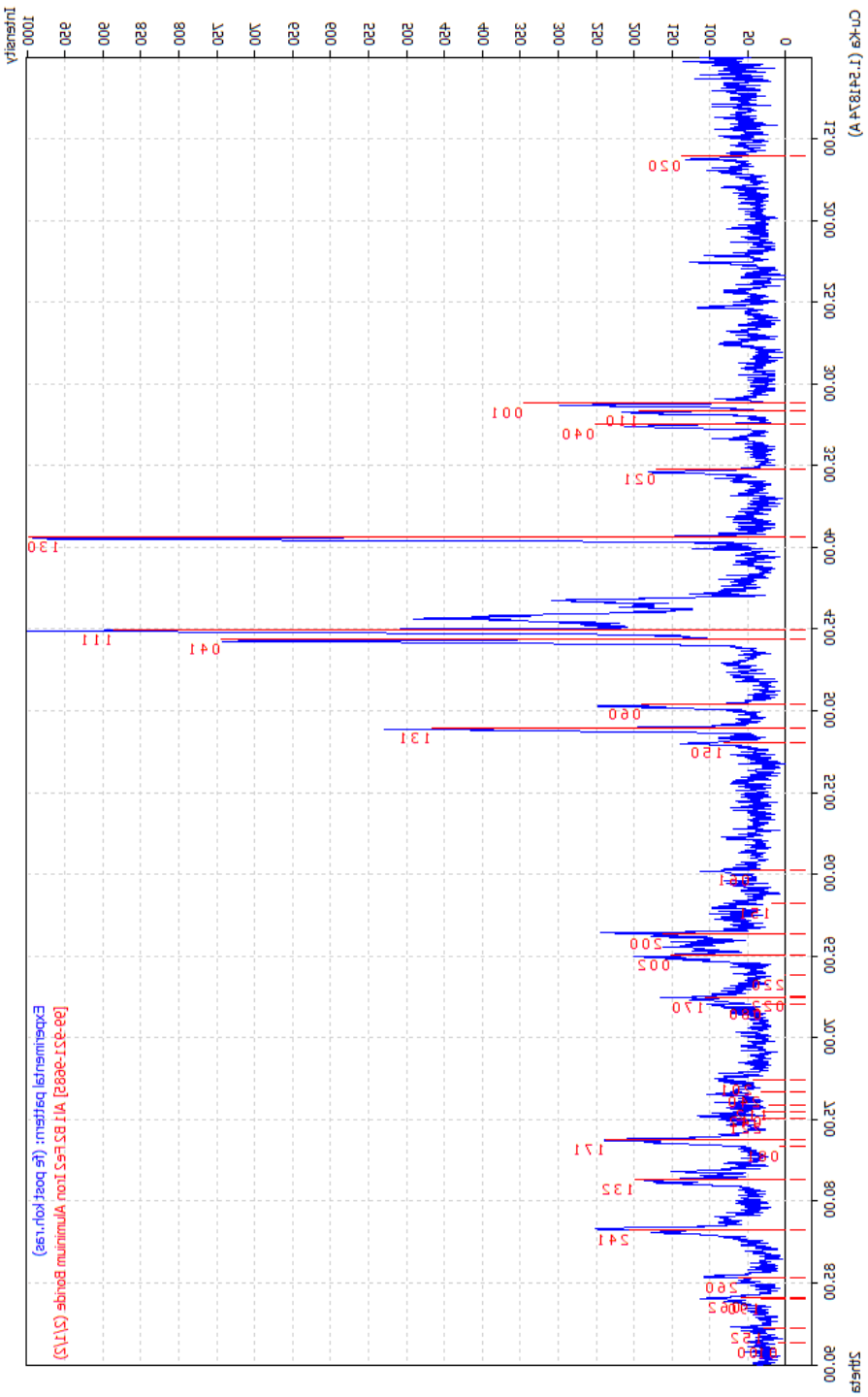

Figure S3.14 XRD diffractograms for Fe_2AlB_2 samples post etching with KOH. Compared to the NaOH sample, the change is much less dramatic, and the majority phase, Fe_2AlB_2, is easily identifiable.

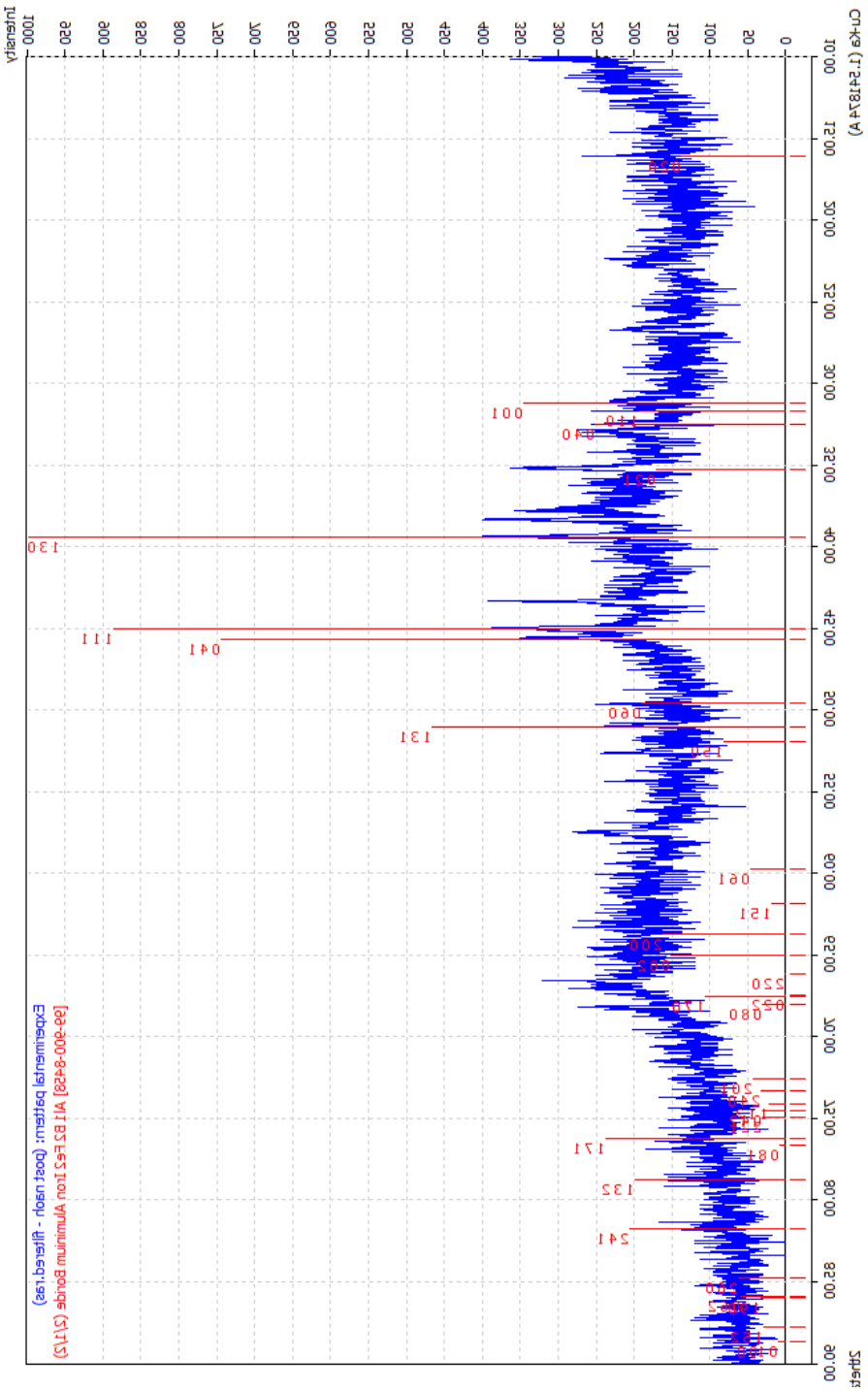

Figure S3.15 XRD diffractograms for Fe_2AlB_2 samples treated with NaOH. Instead of washing and centrifuging, then drying as in above, this sample was filtered with filter paper and a Büchner funnel, then dried. The sample has lost a lot of its crystallinity, but compared to Figure # the Fe_2AlB_2 phase is clear and there is no alumina phase present.